

# JOURNAL OF GLACIOLOGY



**CAMBRIDGE**  
UNIVERSITY PRESS

## **An imbalancing act: the dynamic response of the Kaskawulsh Glacier to a changing mass budget**

Journal:	<i>Journal of Glaciology</i>
Manuscript ID	Draft
Manuscript Type:	Article
Date Submitted by the Author:	n/a
Complete List of Authors:	Young, Erik; Simon Fraser University, Department of Earth Sciences Flowers, Gwenn; Simon Fraser University, Earth Sciences Berthier, Etienne; CNRS - University of Toulouse, LEGOS Latto, Rebecca; Simon Fraser University, Department of Earth Sciences
Keywords:	Glacier mass balance, Ground-penetrating radar, Ice and climate, Melt - surface, Mountain glaciers
Abstract:	<p>The Kaskawulsh Glacier is an iconic outlet draining the icefields of the St. Elias Mountains in Yukon, Canada. We determine and attempt to interpret its catchment-wide mass budget since 2007. Using SPOT5/6/7 data we estimate a 2007--2018 geodetic balance of <math>-0.46 \pm 0.17</math> m w. e.a<sup>-1</sup>. By comparing computed balance fluxes with observed ice fluxes at nine flux gates we examine the discrepancy between the climatic mass balance and internal mass redistribution by glacier flow. Balance fluxes are computed using a fully distributed mass-balance model driven by downscaled and bias-corrected climate-reanalysis data. Observed fluxes are calculated using NASA ITS_LIVE surface velocities and glacier cross-sectional areas derived from ice-penetrating radar data. We find the glacier is still in the early stages of dynamic adjustment to its mass imbalance. We estimate a committed terminus retreat of ~23 km under the 2007-2018 climate and a lower bound of 46 km<sup>3</sup> of committed ice loss, equivalent to ~15% of the total glacier volume. By combining our observations and model output using the continuity equation, we highlight challenges and opportunities in exploring the mass budget of</p>

	large land-terminating glaciers.

SCHOLARONE™  
Manuscripts

# 1 An imbalancing act: the dynamic response of the Kaskawulsh 2 Glacier to a changing mass budget

3 Erik M. YOUNG<sup>1</sup>, Gwenn E. FLOWERS<sup>1</sup>, Etienne BERTHIER<sup>2</sup>, Rebecca LATTO<sup>1\*</sup>

4 <sup>1</sup>*Department of Earth Sciences, Simon Fraser University, 8888 University Drive, Burnaby, British  
5 Columbia, V5A 1S6, Canada*

6 <sup>2</sup>*CNRS, Université de Toulouse, LEGOS, 14 avenue Ed. Belin, Toulouse 31400, France*

7 **ABSTRACT.** The Kaskawulsh Glacier is an iconic outlet draining the icefields  
8 of the St. Elias Mountains in Yukon, Canada. We determine and attempt  
9 to interpret its catchment-wide mass budget since 2007. Using SPOT5/6/7  
10 data we estimate a 2007–2018 geodetic balance of  $-0.46 \pm 0.17$  m w.e. a<sup>-1</sup>.  
11 By comparing computed balance fluxes with observed ice fluxes at nine flux  
12 gates we examine the discrepancy between the climatic mass balance and  
13 internal mass redistribution by glacier flow. Balance fluxes are computed using  
14 a fully distributed mass-balance model driven by downscaled and bias-corrected  
15 climate-reanalysis data. Observed fluxes are calculated using NASA ITS\_LIVE  
16 surface velocities and glacier cross-sectional areas derived from ice-penetrating  
17 radar data. We find the glacier is still in the early stages of dynamic adjustment  
18 to its mass imbalance. We estimate a committed terminus retreat of  $\sim 23$  km  
19 under the 2007–2018 climate and a lower bound of  $46 \text{ km}^3$  of committed ice loss,  
20 equivalent to  $\sim 15\%$  of the total glacier volume. By combining our observations  
21 and model output using the continuity equation, we highlight challenges and  
22 opportunities in exploring the mass budget of large land-terminating glaciers.

---

\*Present address: Mathematics and Physics, University of Tasmania, Private Bag 37, Hobart Tasmania 7001, Australia

## 23 INTRODUCTION

24 The global population of glaciers has been identified as a key contributor to recent (Gardner and others, 2013;  
25 Vaughan and others, 2013; Zemp and others, 2019) and near-future projected sea-level rise (s.l.r.) (Meier  
26 and others, 2007; Radić and others, 2014; Hock and others, 2019), with minimum projected contributions of  
27  $94\pm 25$  mm of s.l.r. from 2010–2100 under the IPCC-AR5 RCP 2.6 scenario (Hock and others, 2019). Outside  
28 of the glaciers peripheral to the Greenland and Antarctic ice sheets, mass loss from glaciers in Arctic Canada  
29 and the Alaska–Yukon region dominates recent and projected sea-level rise (Radić and others, 2014; Wouters  
30 and others, 2019; Zemp and others, 2019). The  $25,267\text{ km}^2$  ice cover of the St. Elias Mountains (Kienholz  
31 and others, 2015) accounts for  $\sim 38\%$  of ice-covered area in the Alaska–Yukon region (Pfeffer and others,  
32 2014), and comprises the largest non-polar icefield in the world. Estimates of mass balance rates in this area  
33 range from  $-0.47\pm 0.09\text{ m w.e. a}^{-1}$  (1962–2006) for the St. Elias and Wrangell Mountains together (Berthier  
34 and others, 2010), to  $-0.63\pm 0.09\text{ m w.e. a}^{-1}$  (2003–2007) for the St. Elias Mountains alone (Arendt and  
35 others, 2008), to  $-0.78\pm 0.34\text{ m w.e. a}^{-1}$  (1958–2008) for glaciers confined to Yukon (Barrand and Sharp,  
36 2010). In addition to their longstanding cultural and historical significance (Cruikshank, 2001), glaciers of  
37 Yukon’s St. Elias Mountains have motivated scientific research dating back to 1935 (Clarke, 2014).

38 This study focuses on the Kaskawulsh Glacier, a large land-terminating glacier on the continental side  
39 of the St. Elias Mountains. Recent retreat of the Kaskawulsh Glacier has had a cascade of unanticipated  
40 consequences, beginning with the 2016 rerouting of runoff destined for the Bering Sea to the Gulf of Alaska  
41 (Shugar and others, 2017). This hydrological reorganization has directly impacted local communities through  
42 metres of lowering of downstream Lhú’áán Män (Kluane Lake) (e.g. McKnight, 2017) and degradation of  
43 local air quality arising from dust mobilized from the abandoned Ä’äy Chú (Slims River) valley (Bachelder  
44 and others, 2020). In addition to its profound effects on local hydrology, the Kaskawulsh Glacier is also an  
45 excellent indicator of regional glacier change: it represents  $\sim 9\%$  of glacier-ice volume in Yukon (Farinotti  
46 and others, 2019), and experienced rates of mass loss from 1977–2007 nearly identical to those calculated  
47 for the St. Elias Mountains as a whole (Berthier and others, 2010). It is also an ideal target for geodetic  
48 mass-balance measurements, being one of few large glaciers in the region not known to surge (Post, 1969)  
49 and therefore free of the complications associated with rapid, large-scale mass redistribution (e.g. Arendt  
50 and others, 2008).

51 New geodetic and geophysical data present a unique opportunity to investigate a decade of change over  
52 the Kaskawulsh Glacier. The first objective of this study is therefore to compute the geodetic mass balance



53 using recently acquired SPOT6/7 data to assess glacier health. The second objective is to assess the state  
54 of dynamic adjustment to the mass (im)balance and to estimate committed mass loss from the Kaskawulsh  
55 Glacier. We do this by comparing measured ice fluxes—estimated using data from the first spatially extensive  
56 ice-penetrating radar survey of the glacier and NASA MEaSURES ITS\_LIVE surface velocities (Gardner  
57 and others, 2019)—to balance fluxes determined using a fully distributed mass-balance model. Hence, we  
58 explore discrepancies between internal mass redistribution and climate-driven surface mass balance change  
59 to evaluate the current extent of this dynamic adjustment. The final objective of this study is to use the  
60 continuity equation to critically evaluate modelled, observed and derived quantities used to compute the  
61 mass budget.

## 62 STUDY AREA

63 The St. Elias Mountains (Figure 1) are characterized by steep elevation gradients, with terrain extending  
64 from sea level in the Gulf of Alaska to some of the highest peaks in North America over less than  
65 100 kilometers. This topographic setting results in steep environmental gradients (e.g. Clarke and  
66 Holdsworth, 2002) due to orographic interruption of atmospheric moisture transport and elevation-  
67 dependent temperature lapse rates (e.g. Marcus and Ragle, 1970; Williamson and others, 2020). These  
68 variable environmental conditions are associated with a full spectrum of glacier thermal and dynamic  
69 regimes, including a significant population of surge-type glaciers (e.g. Post, 1969; Clarke and others, 1986).

70 The Kaskawulsh Glacier is  $\sim 70$  km long, has an area of  $1096 \text{ km}^2$  and comprises three major branches  
71 (referred to as the North, Central and South Arms). One large tributary (Stairway Glacier) merges between  
72 the confluences of the South and Central Arms, while one smaller unnamed tributary joins the Central  
73 Arm above Stairway Glacier and has been known to surge (Foy and others, 2011). The glacier flows  
74 generally eastward from its divides in the Icefield Ranges (at elevations of 2578 m a.s.l., 2091 m a.s.l. and  
75 2393 m a.s.l., respectively, for the North, Central and South Arms). The glacier terminus sits at an elevation  
76 of  $\sim 759$  m a.s.l. at the head of two major river valleys: the Ä'äy Chú (Slims River), which flows north  
77 to Lhú'áán Män (Kluane Lake), and the Kaskawulsh River, which flows southeast to its confluence with  
78 the Alsek River. The  $3027 \text{ km}^2$  Kaskawulsh Glacier catchment also includes numerous smaller glaciers at  
79 elevations ranging from  $\sim 800$  m a.s.l. to  $\sim 3500$  m a.s.l. The Kaskawulsh Glacier is currently retreating, with  
80 its Holocene maximum located approximately 25 km to the north and occurring in the early- to mid-  
81 17th century (Johnson, 1972; Reyes and others, 2006). Foy and others (2011) estimate 1–2 km of retreat  
82 since 1955 using satellite imagery and historical air photos. The most recent estimate of glacier-wide mass

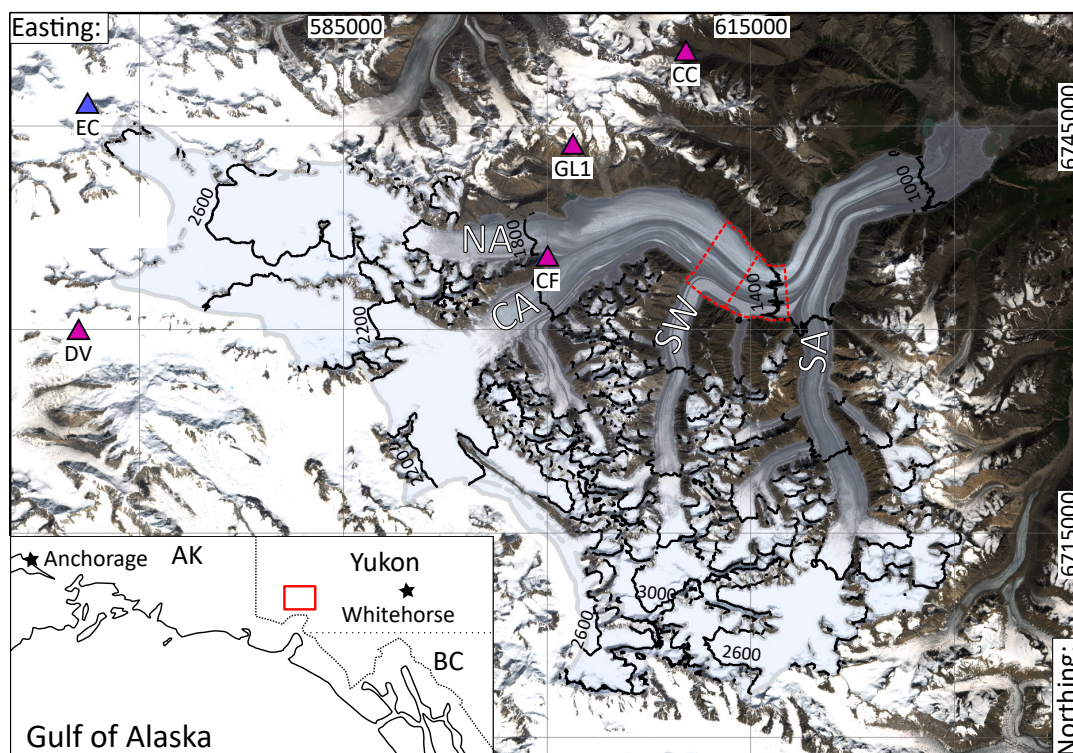


**Fig. 1.** Study area (red box, inset) and overview of Kaskawulsh Glacier. Kaskawulsh Glacier highlighted in blue, with major tributaries labelled: North Arm (NA), Central Arm (CA), Stairway Glacier (SW), South Arm (SA). Also shown are locations of automatic weather stations (magenta triangles) and Eclipse Icefield site with multi-annual accumulation data (blue triangle) (Kelsey and others, 2012). Red dashed lines indicate position of balance terminus position, referred to in the Analysis and Interpretation section. Black contours are metres a.s.l. and coordinates are UTM Zone 7 North. Background image: Copernicus Sentinel data 2017. Retrieved from Copernicus Open Access Hub 01/11/17.

83 balance is  $-0.35 \text{ m w.e. a}^{-1}$  ( $-0.37 \text{ Gt a}^{-1}$ ) for 1995–2013 made using airborne laser altimetry (Larsen and  
 84 others, 2015). Though it has never been thoroughly studied, the thermal regime of Kaskawulsh Glacier  
 85 has been described as temperate (e.g. Foy and others, 2011; Darling, 2012; Herdes, 2014) likely based on  
 86 measurements of ice temperature at depths of 15–24 m (Holdsworth, 1965; Anderton, 1967, 1973), though  
 87 there is evidence of both temperate and polythermal ice in the accumulation area (Holdsworth, 1965).

## 88 GEODETIC MASS BALANCE, 2007–2018

89 Elevation changes and mass balance from 2007 to 2018 are derived from optical satellite stereo-imagery  
 90 acquired by the SPOT5-HRS, SPOT6 and SPOT7 sensors. The 2007 topography is derived by mosaicking  
 91 two SPOT5 DEMs acquired during the SPIRIT project (Korona and others, 2009) on 3 and 13 September

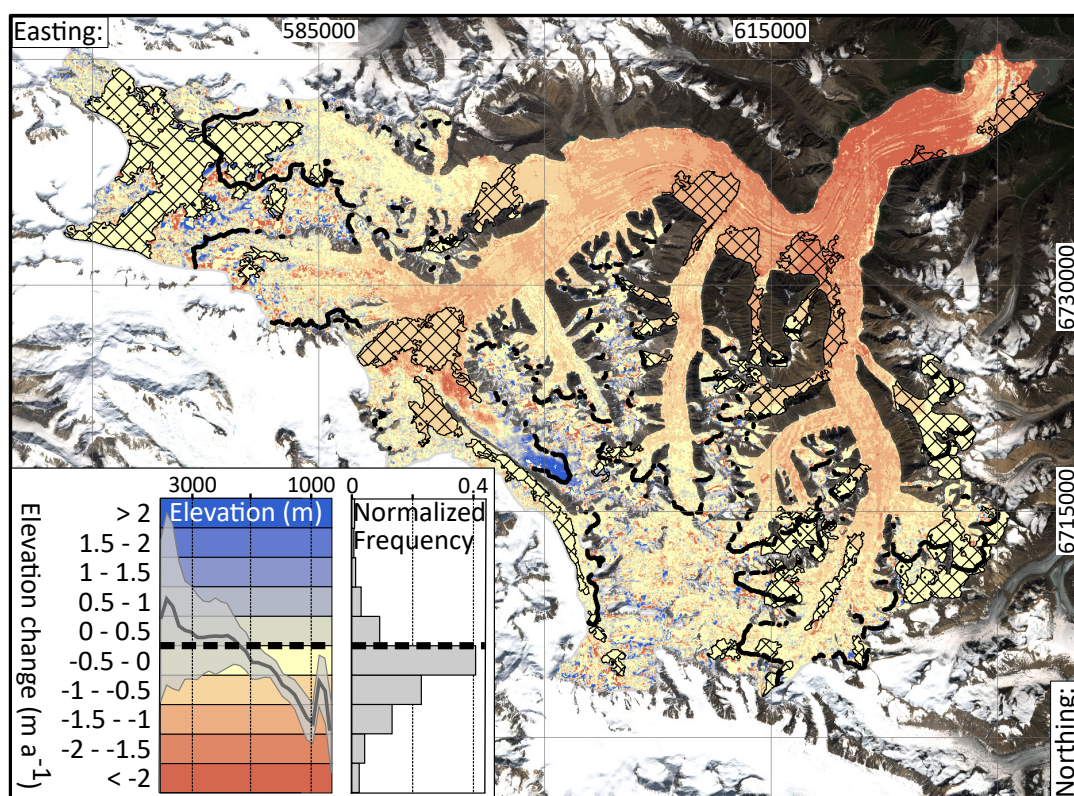


**Fig. 2.** Elevation change of Kaskawulsh Glacier, 2007–2018, derived from SPOT5-HRS, SPOT6/7 optical stereo imagery. Hatched areas indicate interpolated values for gaps  $>1 \text{ km}^2$ . The bold black line corresponds to zero elevation change. Coordinates are UTM Zone 7 North. Inset shows colour scale overlain by elevation change vs elevation (dark grey line = mean, light grey shading = standard deviation) calculated with 100 m elevation bins (left) and histogram of elevation-change (right). Background image: Copernicus Sentinel data 2017. Retrieved from Copernicus Open Access Hub 01/11/17.

92 2007. The 2018 topography is derived from SPOT6 and SPOT7 DEMs acquired on 17 and 31 August, 18  
 93 September and 1 October 2018. We generate SPOT6/7 DEMs using the Ames Stereo Pipeline (Lacroix,  
 94 2016; Shean and others, 2016; Berthier and Brun, 2019).

95 The processing of the DEMs follows the workflow presented in Berthier and Brun (2019). A horizontal  
 96 pixel size of 20 m is chosen here for the analysis. All DEMs are coregistered to TanDEM-X (Rizzoli and  
 97 others, 2017) on stable terrain following Berthier and others (2007), masking out glacierized areas using the  
 98 Randolph Glacier Inventory (RGI) v6.0 (Pfeffer and others, 2014; Kienholz and others, 2015). In 2007, the  
 99 3 September DEM is preferred because it covers most of Kaskawulsh Glacier; its gaps are filled using the  
 100 13 September DEM. In 2018, the 1 October DEM is the primary source of elevation data with successive  
 101 gaps filled by the 17 August, 31 August and 19 September DEMs.

102 To extract elevation change with altitude and compute the mass balances of individual glaciers, we exclude  
 103 data outside  $\pm 3$  standard deviations from the mean elevation difference in each 50 m altitude interval for  
 104 each glacier (Berthier and others, 2004). We also exclude pixels where the surface slope, calculated from  
 105 the TanDEM-X DEM, is larger than  $45^\circ$ . The total volume change is calculated as the integral of the mean  
 106 elevation difference in each 50 m band over the total area–altitude distribution. The mass balances are  
 107 then derived using a volume-to-mass conversion factor of  $850 \text{ kg m}^{-3}$  (Huss, 2013) and dividing by the time  
 108 interval (11 years in this case).

109 Errors in elevation difference are estimated based on the residuals in the overlapping area of the  
 110 coregistered 2007 and 2018 DEMs, a method referred to as triangulation (Nuth and Kääb, 2011; Paul and  
 111 others, 2015). We find mean absolute residuals of  $\sim 1.2 \text{ m}$ , which, given the 11-year time interval, translate  
 112 into  $0.11 \text{ m a}^{-1}$ . Given the size of Kaskawulsh Glacier, we assume that random errors are negligible. The  
 113 spatial coverage with valid elevation-change measurements reached  $\sim 70\%$ . To account for uncertainties due  
 114 to gap filling, we conservatively multiply these errors by a factor of five for the remaining 30% of the area  
 115 (Berthier and others, 2014). An uncertainty of  $\pm 60 \text{ kg m}^{-3}$  is assumed for the volume-to-mass conversion  
 116 factor (Huss, 2013).

117 Figure 2 illustrates nearly pervasive thinning of the Kaskawulsh Glacier from 2007–2018 that generally  
 118 decreases with elevation. The maximum thinning rates exceed  $7.5 \text{ m w.e. a}^{-1}$  roughly 5–10 km upglacier  
 119 of the terminus. The influence of medial moraines is evident in the map of elevation change, but there  
 120 does not appear to be a simple relationship between debris cover and glacier thinning. While it may be  
 121 tempting to ascribe some of the reduced thinning near in the lowermost 5 km of the glacier to debris cover,  
 122 this relationship is not easily corroborated elsewhere. The most notable exception to the observation of  
 123 pervasive thinning is an area of pronounced thickening in the upper reaches of the tributary to the Central  
 124 Arm that is known to surge (Foy and others, 2011), and is likely building up mass during its quiescent  
 125 phase. Heterogeneous patches of thinning and thickening occur at elevations above 1900 m a.s.l. in the  
 126 four tributaries. The data in Figure 2 yield a 2007–2018 average glacier-wide geodetic mass balance of  
 127  $-0.46 \pm 0.17 \text{ m w.e.}$

## 128 MODELLED SURFACE MASS BALANCE

We model the three-hourly distributed surface mass balance  $\dot{b}_{\text{sfc}}(x, y)$  of the Kaskawulsh Glacier as

$$\dot{b}_{\text{sfc}} = \dot{c}_{\text{sfc}} - \dot{a}_{\text{sfc}}, \quad (1)$$



129 where  $\dot{c}_{\text{sfc}}(x, y)$  is the distributed surface accumulation rate and  $\dot{a}_{\text{sfc}}(x, y)$  is the distributed surface ablation  
 130 rate. Modelling the surface mass balance requires four steps (Figure 2): (1) assembling the geometric,  
 131 meteorological and field data used as model inputs, (2) calculating radiation, and downscaling/bias-  
 132 correcting precipitation and temperature, (3) tuning the melt model using observational targets and (4)  
 133 calculating the surface mass balance and its uncertainty for the study time period (Figure 3).

### 134 Mass-balance model

135 We assume that surface ablation is equivalent to melt, which is determined using an enhanced temperature-  
 136 index model originally developed by Hock (1999) that incorporates calculated potential direct clear-  
 137 sky radiation. We drive the melt model with downscaled and bias-corrected regional reanalysis air-  
 138 temperature data. Accumulation is determined by downscaling and bias correcting regional reanalysis  
 139 surface precipitation data, which are then partitioned into rain and snow using a prescribed rain-to-snow  
 140 threshold temperature.

#### 141 Ablation

Melt ( $M$ ) is calculated as (Hock, 1999)

$$M = \begin{cases} (MF + a_{\text{snow/ice}}I) T & T > 0^\circ\text{C} \\ 0 & T \leq 0^\circ\text{C} \end{cases}, \quad (2)$$

142 where  $T$  is the three-hourly temperature obtained from downscaled temperature and geopotential data  
 143 (described below) across the Kaskawulsh Glacier catchment,  $I$  is the potential direct clear-sky radiation,  
 144  $MF$  is the melt factor and  $a_{\text{snow/ice}}$  are the radiation factors for snow and ice, respectively.  $MF$  and  $a_{\text{snow/ice}}$   
 145 must be empirically determined.

#### 146 Accumulation

A statistical downscaling approach adapted from Guan and others (2009) is applied to the regional reanalysis  
 surface precipitation input, with a prescribed rain-to-snow temperature threshold (e.g. Sælthun, 1996;  
 Kienzle, 2008; Clarke and others, 2015) of  $1^\circ\text{C}$  (Johannesson and others, 1995). This threshold value is  
 selected to reduce the difference between modelled and measured accumulation at multiple snow depth and  
 density measurement locations throughout the study time period (considering threshold values of  $0\text{--}2^\circ\text{C}$ ).  
 Refreezing of melt water within the seasonal snow pack is accounted for by implementing a distributed  
 thermodynamic parameterization adapted from Janssens and Huybrechts (2000): for every hydrologic year

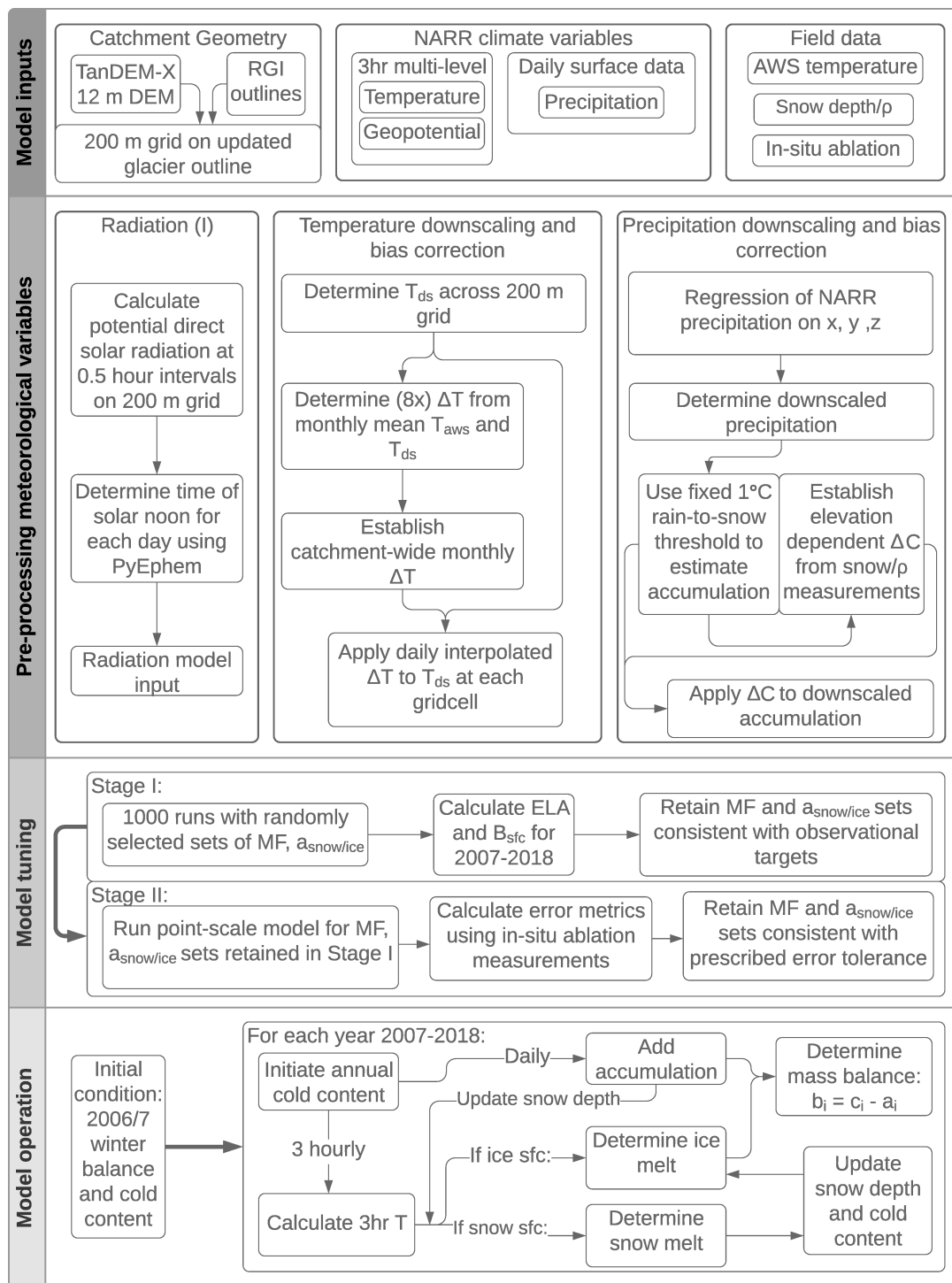


**Fig. 3.** Mass-balance model workflow, including (from top to bottom) assembly of model inputs, pre-processing of meteorological variables, model tuning and using the tuned model to calculate mass balance.

in the study time period, total energy consumed by refreezing is approximated as a proportion ( $P_r$ ) of the seasonal snow pack:

$$P_r = \frac{c}{L} \max(T_{\text{mean}}, 0) \frac{d}{C_{\text{mean}}}, \quad (3)$$

147 with  $c$  the specific heat capacity of ice,  $L$  the latent heat of fusion,  $T_{\text{mean}}$  the local mean annual air  
148 temperature ( $^{\circ}\text{C}$ ),  $C_{\text{mean}}$  the local mean annual accumulation for the study time period and  $d$  the thickness  
149 of the thermal active layer raised to the melting point by refreezing. The value of  $d$  is set to 2 m (Oerlemans,  
150 1991; Janssens and Huybrechts, 2000), which has been used for the parameterization of refreezing in  
151 modelling studies of glaciers in Western Canada (Clarke and others, 2015).

## 152 **Model inputs**

### 153 *Digital elevation model and glacier geometry*

154 We use the TanDEM-X radar satellite Digital Elevation Model (DEM) product (Krieger and others, 2007)  
155 resampled to 200 m to define the grid on which mass-balance calculations are performed. The Kaskawulsh  
156 Glacier outline from the Global Land Ice Measurements from Space inventory (GLIMS) (Raup and others,  
157 2007; RGI Consortium, 2017) is modified to match catchment boundaries derived from applying the Arc  
158 GIS 10.7 Hydrology toolbox basin delineation tools to the TanDEM-X DEM (resulting in a 4% increase in  
159 area from 1054 to 1096 km<sup>2</sup>).

### 160 *Debris cover mask*

161 To account for the effects of debris cover on modelled mass balance, we first generate a debris-cover mask  
162 using imagery from Sentinel-2 band 12 (central wavelength 2202.2 nm, 20 m spatial resolution) on 1 August  
163 2017. Infrared bands of the Sentinel-2 product produce a clear contrast between debris-covered and debris-  
164 free ice on cloudless summer days when debris temperature is elevated due to unobstructed radiative heating  
165 (e.g. Nakao, 1982). Cold (darker) and warm (lighter) pixels are automatically classified based on greyscale  
166 value (derived from the original RGB values) and converted to a binary debris mask raster. A debris-cover  
167 boolean is assigned to each grid cell by resampling the debris mask raster to the 200 m model grid. The mask  
168 fails to capture some debris-covered cells in direct contact with a pro-glacial lake encircling the terminus.  
169 Here the presumptive effects of ice–water interactions are expected to compensate for the lack of modelled  
170 debris shielding.

### 171 *Potential direct clear-sky radiation*

172 Potential direct clear-sky radiation  $I$  (Equation 2) is calculated at 0.5 h intervals using a combination  
173 of the ArcGIS Solar Analyst toolbox and a custom adaptation of the python PyEPHEM astronomical  
174 calculations module to assign local time to the calculated radiation values (see Supplementary Materials).  
175 Radiation is calculated across the 200 m grid for clear-sky conditions by incorporating a fixed atmospheric

176 transmissivity of 0.75 (Hock, 1998, 1999). The time of solar noon for each grid cell in the domain is computed  
177 using PyEPHEM. The median time of insolation in modelled solar radiation values are assigned to the  
178 computed solar noon times in order to correctly assign timestamps to the modelled values. The modelled  
179 solar geometry does not incorporate changes in atmospheric transmissivity, making the calculated radiation  
180 values insufficient for modelling mass balance several decades into the past or future (Wild and others, 2005;  
181 Huss and others, 2009), but adequate for modelling mass balance over multiple successive years. This use  
182 of calculated radiation values conforms with the observation of minimal sensitivity of ablation to temporal  
183 changes in the potential solar radiation on multi-annual timescales (Vincent and Six, 2013).

#### 184 *Meteorological variables*

185 Temperature and precipitation inputs to the downscaling routine (described below) are obtained from the  
186 National Centre for Environmental Prediction's (NCEP) North American Regional Reanalysis (NARR)  
187 product (Mesinger and others, 2006). The NARR product comprises multiple atmospheric and surface  
188 climate variables at high temporal (3 hourly) and moderate spatial (32 km at 60° N) resolution for the  
189 North American continent between 1979 and present. Three-hourly temperature and geopotential data at  
190 29 discrete pressure levels in the atmosphere are used as inputs for the temperature downscaling. Daily  
191 total surface precipitation data are used as inputs for the precipitation downscaling.

### 192 **Downscaling and bias correction of meteorological variables**

#### 193 *Temperature*

194 Temperature downscaling follows an approach that reconstructs the temperature profile in the lower  
195 atmosphere using a linear interpolation scheme (Jarosch and others, 2012). At each NARR grid point local  
196 lapse rates and sea-level air temperature values are determined by using a linear regression to correlate  
197 temperature and geopotential heights, for heights associated with pressures greater than 300 hPa. The  
198 resulting lapse rates (slopes) and sea-level air temperatures (intercepts) are bilinearly interpolated across  
199 the model domain at 200 m spacing. Two-metre air temperature is then calculated on the 200 m model grid  
200 using the local lapse rate and sea-level temperature. Changes in the sign of the NARR-derived lapse rates  
201 are monitored to identify inversions, which are treated by calculating independent lapse rates above and  
202 below the inversion height (Jarosch and others, 2012).

Automatic Weather Station (AWS) temperature records are available from four stations belonging to the SFU Glaciology Group, two belonging to the University of Ottawa Laboratory for Cryospheric Research and two operated by Environment Canada. AWS temperature records are used to obtain monthly bias



corrections for the downscaled temperatures (Figure 4). Monthly mean temperatures for each AWS location are determined for the time intervals over which data are available within the study period. The minimum AWS record length is seven years. A  $\Delta$  change method is used to calculate a bias correction (Hay and others, 2000; Clarke and others, 2015):

$$T_c(x, y, t) = T_{ds}(x, y, t) + \Delta T(t), \quad (4)$$

203 where  $T_c(x, y, t)$  is the bias-corrected temperature at position  $x, y$  and time  $t$ ,  $T_{ds}(x, y, t)$  is the temperature  
 204 at the same position and time downscaled from the NARR data and  $\Delta T(t)$  is the difference between the  
 205 mean monthly downscaled temperature and mean monthly AWS temperatures, linearly interpolated to  
 206 daily values. Note that the startling mismatch in downscaled and AWS-measured temperatures occurs for  
 207 the two distal low-elevation stations and occurs only from September to April (largely outside of the melt  
 208 season).

The monthly values of  $\Delta T(t)$  used in Equation 4 are determined by averaging  $\Delta T(t)$  values obtained from individual AWS records, weighted according to the AWS record lengths:

$$\Delta T(t) = \frac{1}{\sum_{i=1}^8 \alpha_i} \sum_{i=1}^8 \alpha_i \Delta T_i(t), \quad (5)$$

209 where  $\Delta T_i(t)$  is the mean monthly value computed using one of the eight AWS records, and the weights  $\alpha_i$   
 210 are proportional to the AWS record lengths. We did not consider using spatially variable values of  $\Delta T(t)$   
 211 due to the sparse and skewed distribution of AWS stations (Figure 4a) and the corresponding need for  
 212 extrapolation.

213 The NARR-derived downscaled and bias-corrected temperatures are compared to AWS records to evaluate  
 214 the temperature input to the model. Prior to this comparison, the AWS records (with five-minute sampling  
 215 interval) are smoothed to three-hourly values and sampled at the times corresponding to the NARR data.  
 216 Both Mean Absolute Error (MAE) and Root Mean Squared Error (RMSE) are computed for monthly mean  
 217 and three-hourly temperatures; the monthly means of the three-hourly MAE/RMSE are also computed.  
 218 For both monthly and three-hourly values, the lowest RMSEs/MAEs are observed in the summer months,  
 219 while highest RMSEs/MAEs occur between September and February (see Supplementary Material). These  
 220 errors show little inter-annual variability when accounting for inter-annual differences in temporal coverage  
 221 between stations: inter-annual standard deviations are 0.33°C (RMSE) and 0.48°C (MAE).

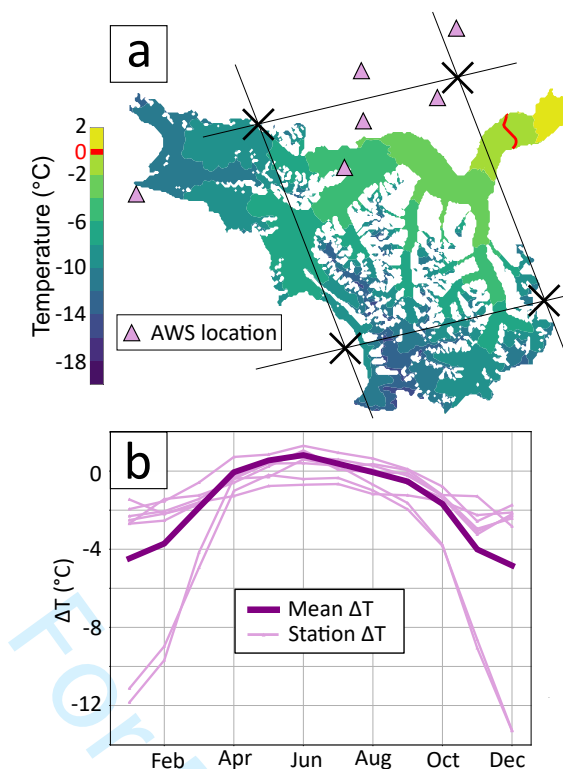


**Fig. 4.** Temperature downscaling and bias correction. (a) Mean 2 m air temperature field for 2007–2018 following downscaling and bias correction of NARR data. Locations of four NARR grid nodes (black crosses) and six AWS (purple triangles) are shown. Environment Canada AWS at Burwash Landing (UTM: 604700 E, 6805731 N) and Haines junction (UTM: 698045 E, 6704555 N) are not shown due to scale. (b) Monthly values of  $\Delta T$  for each AWS (fine pink lines) along with mean monthly  $\Delta T$  used for bias correction of downscaled temperatures (bold purple line). Anomalously low values of  $\Delta T$  are from Burwash Landing and Haines Junction, both a minimum of  $\sim 60$  km from the Kaskawulsh Glacier.

## 222 *Precipitation*

223 Precipitation downscaling is achieved using a regression-based method that incorporates daily total surface  
 224 precipitation at NARR grid points and geographic predictors of precipitation on the 200 m grid (Easting,  
 225 Northing, elevation) (Guan and others, 2005, 2009), but does not include other reanalysis-derived climatic  
 226 variables (c.f Hofer and others, 2017). A rain-to-snow threshold of  $1^{\circ}\text{C}$  is used to calculate accumulation.  
 227 Daily timesteps are used to minimize the influence of local sub-diurnal meteorological effects on precipitation  
 228 variability that significantly weaken the performance of the downscaling method (Guan and others,  
 229 2009). Dynamic downscaling, which uses wind speed and direction to track saturated air masses where  
 230 precipitation occurs (Smith and Barstad, 2004), is not implemented due to increased data requirements and

231 our comparatively small model domain relative to those of studies using a similar strategy for obtaining  
232 distributed mass-balance model inputs (e.g. Jarosch and others, 2012; Clarke and others, 2015).

233 Snow depth and density measurements made 43 times over 13 years at 13 locations on or proximal to  
234 the Kaskawulsh Glacier are used to determine an elevation-dependent bias correction for accumulation  
235 (Figure 5a). We also include published values of winter accumulation from the Eclipse Icefield (Kelsey and  
236 others, 2012). At each location, we calculate the difference between measured ( $C_{\text{obs}}$ ) and downscaled ( $C_{\text{ds}}$ )  
237 seasonal accumulation on the date of measurement. When accumulation measurements are available for  
238 multiple years, the median of the net differences is selected. A linear interpolation of these differences with  
239 site elevation (Figure 5b) is then used to compute the relative (fractional) difference between downscaled  
240 and measured seasonal accumulation to determine the bias-corrected accumulation for each grid cell:

$$C_c(x, y, t) = C_{\text{ds}}(x, y, t) \Delta C(z), \quad (6)$$

241 where  $C_c(x, y, t)$  is the bias-corrected accumulation at position  $x, y$  and time  $t$ ,  $C_{\text{ds}}(x, y, t)$  is the  
242 accumulation at the same position and time downscaled from the NARR precipitation data and  $\Delta C(z)$   
243 is the elevation-dependent bias correction factor (see Supplementary Material). A mean difference of  $0.08$   
244  $\pm 0.24$  m w.e. is calculated using all available accumulation measurements and modelled winter balance  
245 at the corresponding grid cells on the dates of the measurement (with corresponding difference of  $0.65 \pm$   
246  $0.36$  m w.e. if bias correction is omitted).

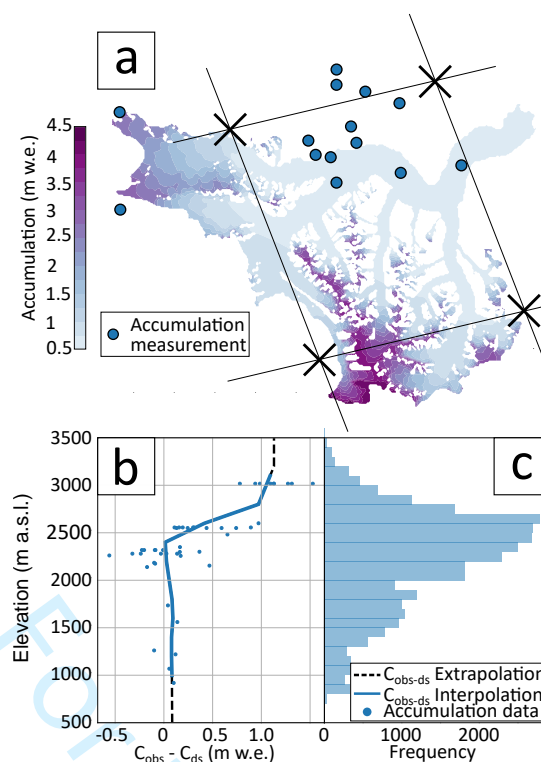


**Fig. 5.** Precipitation downscaling and accumulation bias correction. (a) Mean annual accumulation field for 2007–2018 following downscaling of NARR daily surface precipitation and bias correction of accumulation. Locations of four NARR grid nodes (black crosses) and snow depth/density measurements (blue circles) are shown. Eight additional snow-measurement locations are not shown due to scale. (b) Interpolated (solid blue line) and extrapolated (dashed black line) elevation-dependent values of difference between measured and downscaled accumulation ( $C_{\text{obs}} - C_{\text{ds}}$ ), along with values of  $C_{\text{obs}} - C_{\text{ds}}$  at measurement locations (blue dots). (c) Hypsometry of Kaskawulsh Glacier, with frequency of  $200\text{ m} \times 200\text{ m}$  gridcells in each bin.

## 247 Model tuning

248 Before the mass-balance model can be applied to the Kaskawulsh Glacier, the melt model must be tuned  
 249 to empirical targets to determine the values of model parameters  $MF$  and  $a_{\text{snow/ice}}$  (Equation 2) for both  
 250 debris-free and debris-present cases. The shielding effect of debris cover (e.g. Reznichenko and others, 2010)  
 251 is crudely represented (in the debris-present case) by setting radiation parameters  $a_{\text{snow/ice}}$  to zero in all  
 252 debris-covered cells.

## 253 Observational targets

254 We use an estimated geodetic glacier-wide mass balance rate of  $-0.46 \pm 0.17\text{ m w.e. a}^{-1}$  (see above), 144  
 255 in-situ ablation measurements and empirically derived snowline elevations for the Kaskawulsh Glacier to  
 256 tune the melt model. In-situ ablation measurements were made at 44 point locations over 144 time intervals

257 (ranging in length from 12 to 136 days) at multiple field sites, including two small alpine glaciers and the  
258 Kaskawulsh Glacier itself (see Figure 6b for locations). Net ablation is derived from measurements of stake  
259 height and surface density. Snow depth was measured at each stake, while depth-integrated snow density  
260 was usually obtained from snowpit density profiles. We assume an ice density of  $900 \text{ kg m}^{-3}$  to convert  
261 ice-surface lowering to ablation.

262 Equilibrium Line Altitudes (ELAs) are approximated as late-summer snowlines on the four major  
263 tributaries (North Arm, Central Arm, South Arm, Stairway Glacier) of the Kaskawulsh Glacier identified  
264 in Sentinel-2 (2015–2019) or Landsat-8 (2013–2014) imagery (e.g. Pelto and others, 2008). The calendar  
265 dates of the images range from 1 August (2018) to 8 September (2014). The images selected were almost  
266 cloud-free and displayed no evidence of recent snowfall, which is usually readily identifiable on the medial  
267 moraines. For each of the tributaries, three snowlines are picked for each year corresponding to an upper  
268 bound, a lower bound and a reference estimate. The mean snowline elevation for each year is determined  
269 from all three values at all locations free of cloud cover, yielding a 2013–2019 mean of  $2261 \pm 151 \text{ m a.s.l.}$   
270 (one standard deviation). The maximum and minimum annual snowline-elevation estimates at any of the  
271 four locations are  $2477 \text{ m a.s.l.}$  (Central Arm, 4 August 2019) and  $1927 \text{ m a.s.l.}$  (South Arm, 1 August 2018).

### 272 *Tuning approach and results*

273 Model tuning is performed in two stages to determine parameter combinations that produce modelled values  
274 of (1) glacier-wide mass balance and average ELA, and (2) point-scale ablation that match observations  
275 within the assessed uncertainty. Model tuning is performed independently for the debris-free and debris-  
276 present cases. The motivation for the two-stage tuning process arises from the grossly inadequate number  
277 and spatial coverage of available point-scale mass-balance data (see Figure 6b). Tuning a model only to  
278 these data would be misguided at best, and likely yield estimates of glacier-wide mass balance that are  
279 wildly at odds with the observed geodetic balance. We designed the two-stage tuning process to first  
280 eliminate simulations that are incompatible with the geodetic mass balance and observed ELA, and then  
281 take advantage of the point-scale geographically specific data to determine a final set of acceptable model  
282 parameters. Using multiple data sources and error metrics in the tuning process also goes some way toward  
283 addressing the persistent problem of equifinality in these types of models. We include both debris-free and  
284 debris-present cases as a means of evaluating the influence of debris on the spatial distribution of modelled  
285 melt.

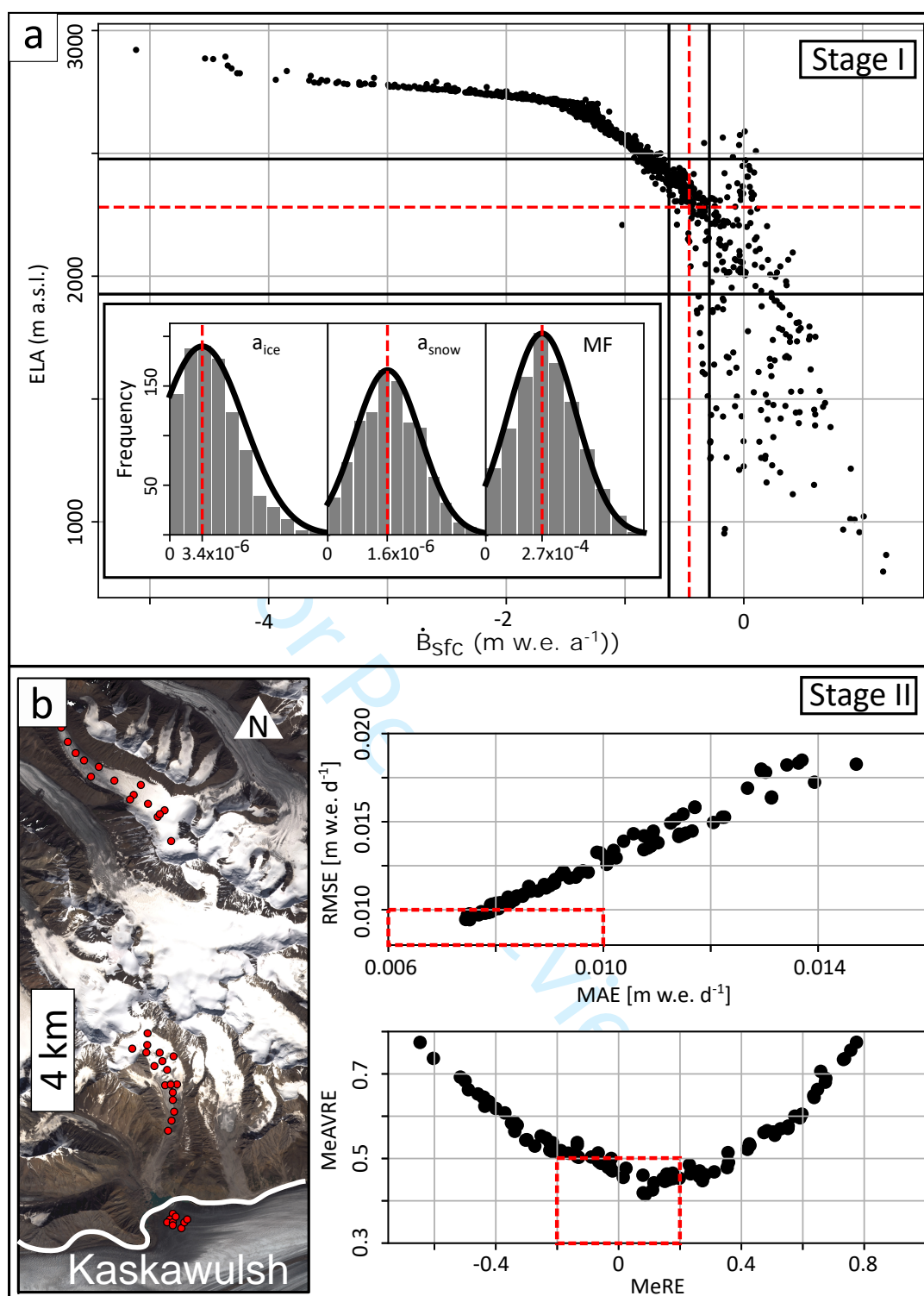


**Fig. 6.** Two-stage model tuning shown for debris-present simulations. The same procedure is carried out for debris-free simulations (see Supplementary Material). (a) Stage 1. Modelled ELA versus glacier-wide mass balance for 2007–2018 for 1000 simulations (black dots) with values of  $MF$  (m w.e.  $3h^{-1} \text{ } ^\circ\text{C}^{-1}$ ),  $a_{ice}$  and  $a_{snow}$  (m w.e.  $3h^{-1} \text{ } ^\circ\text{C}^{-1} \text{ m}^2 \text{ W}^{-1}$ ) randomly selected from normal distributions truncated at zero (inset). Observational targets (red dashed lines) are shown for ELA and glacier-wide mass balance. Simulations falling within the observational uncertainty (black lines) proceed to Stage 2. (b) Stage 2. RMSE versus MAE (top) and median of the absolute value of the relative error (MeAVRE) versus the median of the relative error (MeRE) between modelled and measured net ablation (bottom) at 44 locations (map at left). 12 simulations falling within both red dashed rectangles pass Stage 2.

286 In Stage 1, 1000 random combinations of parameters  $MF$ ,  $a_{ice}$  and  $a_{snow}$  are selected from independent  
287 normal distributions (Figure 6a, inset). These distributions are defined using the mean and standard  
288 deviation of published values of  $MF$ ,  $a_{ice}$  and  $a_{snow}$  from studies employing the same temperature-index melt  
289 model (Hock, 1999):  $2.707 \pm 1.632 \times 10^{-4}$  m w.e.  $3 \text{ h}^{-1} \text{ }^\circ\text{C}^{-1}$  for  $MF$ ,  $3.396 \pm 2.65 \times 10^{-6}$  m w.e.  $3 \text{ h}^{-1} \text{ }^\circ\text{C}^{-1} \text{ m}^2$   
290  $\text{W}^{-1}$  for  $a_{ice}$  and  $1.546 \pm 0.85 \times 10^{-6}$  m w.e.  $3 \text{ h}^{-1} \text{ }^\circ\text{C}^{-1} \text{ m}^2 \text{ W}^{-1}$  for  $a_{snow}$ . The normal distributions are  
291 truncated at zero to ensure positive values of  $MF$ ,  $a_{ice}$  and  $a_{snow}$ . Using each of the 1000 model-parameter  
292 combinations, we calculate the glacier mass balance from 2007–2018 and retain all simulations that meet  
293 two criteria (Figure 6a): (1) modelled mean annual glacier-wide mass balance rate  $\dot{B}_{sfc}$  within the assessed  
294 uncertainty of the 2007–2018 geodetic balance:  $-0.46 \pm 0.17$  m w.e.  $\text{a}^{-1}$ , and (2) modelled ELA that falls  
295 within the range of snowline elevations determined for the main tributaries of the Kaskawulsh Glacier: 1927–  
296 2477 m a.s.l. For the debris-free and debris-present cases, respectively, 92 and 117 parameter combinations  
297 of the 1000 meet both criteria.

298 In Stage 2, we use the parameter combinations retained after Stage 1 to model mass balance corresponding  
299 to in-situ ablation-stake measurements (Figure 6b). These measurements, by their nature, represent the net  
300 rather than the total ablation. We compute the RMSE and MAE between the modelled and measured  
301 ablation (in m w.e.  $\text{day}^{-1}$ ) and retain all simulations with RMSE and MAE  $< 0.01$  m w.e.  $\text{day}^{-1}$  (Figure 6b,  
302 top right). Differences between modelled and measured ablation are normalized based on the length of the  
303 measurement interval. We then calculate the relative error between modelled and measured net ablation for  
304 each of the 144 melt intervals, and retain simulations with a median relative error (MeRE)  $< \pm 20\%$  and  
305 a median of the absolute value of the relative error (MeAVRE)  $< 50\%$  (Figure 6b). A total of 12 and 25  
306 simulations meet all the above criteria for the debris-present and debris-free cases, respectively.

### 307 Mass-balance model results

308 We model 12 and 25 net mass-balance fields for 2007–2018 corresponding to the parameter combinations  
309 that satisfy all the model-tuning conditions above for the debris-free and debris-present cases, respectively  
310 (Figure 7). From these 12 or 25 fields, we compute a mean (reference) field and a field of the associated  
311 standard deviation, which we use as a metric of modelled mass-balance variability. We compute a glacier  
312 wide modelled mean (reference) mass balance of  $-0.49 \pm 0.08$  m w.e.  $\text{a}^{-1}$  and average ELA of  $2254 \pm 80$  m a.s.l.  
313 for the debris-free case, and a modelled mean (reference) mass balance of  $-0.42 \pm 0.10$  m w.e.  $\text{a}^{-1}$  and average  
314 ELA of  $2309 \pm 41$  m a.s.l. for the debris-present case.

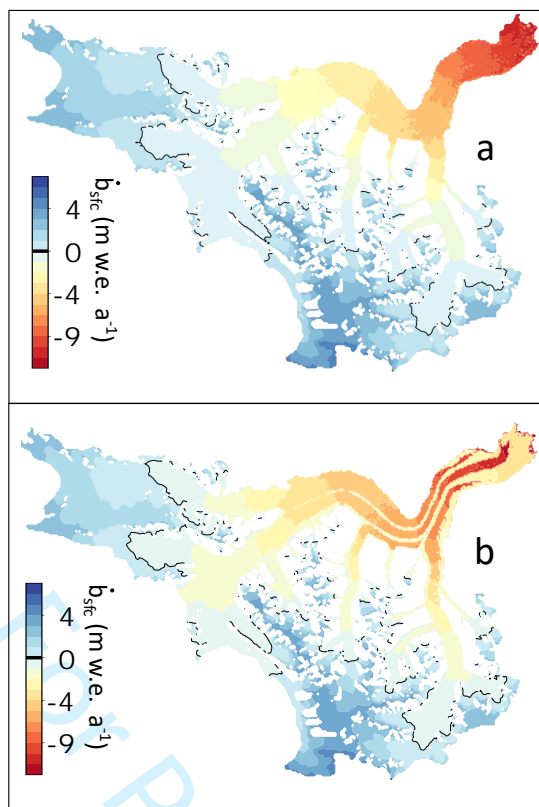


**Fig. 7.** Mass-balance model results. (a) Reference mass-balance field for debris-free case. (b) Same as in (a) but for debris-present case.

315 Uncertainty on the modelled glacier-wide mass balance arises from uncertainty on the modelled melt and  
 316 uncertainty on the downscaled and bias-corrected accumulation. For the melt term we use the standard  
 317 deviation of the modelled melt rates across all 12 or 25 simulations that pass the two-stage tuning as  
 318 the uncertainty  $\delta_{\dot{A}_{\text{sfc}}}$ . For the accumulation term, we use the mean absolute differences between modelled  
 319 and measured values (see accumulation bias correction), normalized by the measured values, to establish  
 320 a relative uncertainty that is applied to the downscaled and bias-corrected accumulation rates to obtain a  
 321 dimensional uncertainty  $\delta_{\dot{C}_{\text{sfc}}}$ . We then compute uncertainty on the mass balance as  $\delta_{\dot{B}_{\text{sfc}}} = \sqrt{\delta_{\dot{A}_{\text{sfc}}}^2 + \delta_{\dot{C}_{\text{sfc}}}^2}$ .

### 322 Balance fluxes

323 Volumetric balance fluxes at each of the nine flux gates (Figure 8, Table 1) are determined from the modelled  
 324 mass-balance fields  $\dot{b}_{\text{sfc}}$  as:

$$Q_{\text{bal}} = \int_A \dot{b}_{\text{sfc}} dA, \quad (7)$$



**Table 1.** Balance fluxes  $Q_{\text{bal}}$ , standard deviations  $\sigma_Q$  and uncertainties  $\delta_Q$  at each flux gate (refer to Figure 8) for debris-present and debris-free cases. Tributary flux gates are: North Arm (NA), Central Arm (CA), Stairway Glacier (SW), South Arm (SA). Flux gates along the main trunk are: KW5 (highest) to KW1 (lowest). All values in  $\text{km}^3 \text{a}^{-1}$ .

Flux gate	Debris-present			Debris-free		
	$Q_{\text{bal}}$	$\sigma_Q$	$\delta_Q$	$Q_{\text{bal}}$	$\sigma_Q$	$\delta_Q$
NA	0.108	0.009	0.038	0.143	0.018	0.041
CA	0.080	0.016	0.054	0.136	0.031	0.058
SW	0.111	0.006	0.025	0.121	0.009	0.025
SA	0.074	0.016	0.046	0.102	0.024	0.048
KW5	0.101	0.030	0.099	0.206	0.059	0.108
KW4	0.018	0.035	0.105	0.135	0.066	0.115
KW3	0.035	0.046	0.137	0.171	0.079	0.147
KW2	-0.081	0.055	0.147	0.051	0.084	0.210
KW1	-0.193	0.087	0.210	-0.070	0.108	0.249

325 where  $A$  is the glacier area upstream of the flux gate of interest. This approach produces 12 and 25 sets  
 326 of balance fluxes at each gate for debris-present and debris-free cases, respectively. The reference balance  
 327 fluxes at each flux gate are the averages of these 12 or 25 values. Uncertainty on the balance fluxes is  
 328 determined directly from uncertainty on the mass-balance field as described above. We also report the  
 329 standard deviation of the balance fluxes from all 12 or 25 simulations to give a sense of the variability.

330 For both debris-free and debris-present cases, balance fluxes are greatest somewhere downstream of the  
 331 North and Central Arm tributaries and decrease thereafter toward the terminus (Table 1). The primary  
 332 differences between balance fluxes derived from the debris-free versus debris-present cases are: (1) the  
 333 debris-free balance fluxes are consistently higher and (2) negative balance fluxes extend further upstream  
 334 (to KW2) for the debris-present case.

### 335 Sensitivity analysis

336 Here we quantify the sensitivity of the modelled mass balance to (1) the temperature and accumulation bias  
 337 corrections, (2) the rain-to-snow temperature threshold and (3) refreezing. We determine the sensitivity of  
 338 the model to each of these components by comparing the glacier-wide mass balance rate  $\dot{B}_{\text{sfc}}$  computed  
 339 from the mean  $\dot{b}_{\text{sfc}}$  fields (using the 25 and 12 parameter combinations for debris-free and debris-present  
 340 cases, respectively) and resulting balance fluxes when each model component is disabled (bias corrections,  
 341 refreezing) or changed (rain-to-snow threshold) (Table 2 and Supplementary Material). Model components

**Table 2.** Sensitivity of glacier-wide mass balance (m w.e. a<sup>-1</sup>) for debris-free and debris-present cases to: disabling temperature bias correction (No  $\Delta T$ ), disabling accumulation bias correction (No  $\Delta C$ ), disabling refreezing parameterization (No RF) and changing rain-to-snow threshold temperature ( $T_{R2S}$ ). For each test and the reference runs, glacier-wide mass balance  $\dot{B}_{sfc}$  and standard deviation  $\sigma_{\dot{B}_{sfc}}$  are given in m w.e. a<sup>-1</sup>

Test	Debris-free		Debris-present	
	$\dot{B}_{sfc}$	$\sigma_{\dot{B}_{sfc}}$	$\dot{B}_{sfc}$	$\sigma_{\dot{B}_{sfc}}$
Reference	-0.49	0.08	-0.42	0.10
No $\Delta T$	-0.48	0.08	-0.36	0.12
No $\Delta C$	-1.43	0.09	-1.24	0.11
No RF	-0.99	0.13	-0.81	0.13
$T_{R2S} = 0^\circ\text{C}$	-0.53	0.09	-0.46	0.10
$T_{R2S} = 2^\circ\text{C}$	-0.44	0.09	-0.38	0.10

342 are disabled/changed independently, thus we do not evaluate their interdependence. Changes in  $\dot{B}_{sfc}$  are  
 343 similar for both debris-free and debris-present simulations, except in the case of the temperature bias  
 344 correction.

#### 345 *Accumulation bias correction*

346 Disabling the accumulation bias correction triples the mass loss (decreasing  $\dot{B}_{sfc}$ ), the largest response of all  
 347 sensitivity tests. The resulting balance fluxes are negative at all gates due to the strong elevation dependence  
 348 of the accumulation bias correction, including the marked increase in  $\Delta C$  at elevations  $> 2300$  m a.s.l.  
 349 (Figure 5b). With 52% of the glacier area above 2300 m a.s.l. (Figure 5c), the bias correction produces  
 350 accumulation increases of 2–5 times over a significant area. The gap between measured and downscaled  
 351 NARR accumulation speaks to the necessity of applying a bias correction. However, it is important to note  
 352 that the high-elevation data used for this bias correction come from the western margin of the catchment  
 353 (North/Central Arms), rather than the southern margin (Stairway Glacier/South Arm) where much of the  
 354 high-elevation terrain is found. The bias correction is thus unconstrained in the area where it has the largest  
 355 impact, and its effects must therefore be interpreted with caution.

#### 356 *Temperature bias correction*

357 Disabling the temperature bias correction increases  $\dot{B}_{sfc}$  by  $< 0.01$  m w.e. a<sup>-1</sup> and  $0.06$  m w.e. a<sup>-1</sup> for the  
 358 debris-free and debris-present cases, respectively (with correspondingly small changes to balance fluxes).  
 359 This small change in  $\dot{B}_{sfc}$  is the result of averaging positive and negative anomalies arising from the 25

360 debris-free cases, and mostly positive but small anomalies for the 12 debris-present cases. The temperature  
361 bias correction results in modest increases in mid-April to mid-August temperatures, but marked to drastic  
362 decreases in temperatures during the rest of the year (Figure 4b). Therefore, with the bias correction applied,  
363 PDDs increase during much of the melt season but decline in the shoulder seasons. Accumulation is also  
364 affected via the rain-to-snow threshold temperature, with less accumulation from mid-April to mid-August  
365 but more otherwise. Overall, the model sensitivity to temperature bias correction is minimal, producing  
366 an order of magnitude lower impact on  $\dot{B}_{\text{sfc}}$  compared to disabling the accumulation bias correction or  
367 refreezing.

### 368 *Refreezing model and rain-to-snow threshold*

369 Disabling the refreezing parameterization causes an earlier seasonal transition from snow to ice, and thus an  
370 increase in melt owing in part to the higher radiation factors for ice compared to snow ( $a_{\text{ice/snow}}$ ), resulting  
371 in an approximate doubling of mass loss. Disabling refreezing also increases the frequency and intensity of  
372 mid-winter melt events caused by positive temperatures, in some cases depleting the snowpack entirely and  
373 exposing the underlying ice. The widespread nature of these modelled mid-winter ablation events that occur  
374 when refreezing is disabled are considered unrealistic. We also test the model sensitivity to rain-to-snow  
375 thresholds of 0 and 2°C, bracketing the reference value of 1°C. These values produce variations in modelled  
376  $\dot{B}_{\text{sfc}} < \pm 0.05$  m w.e. a<sup>-1</sup> for both debris-free and debris-present cases.

## 377 **ICE FLUXES**

378 We use new ice-penetrating radar data, along with the NASA MEaSUREs ITS\_LIVE surface velocities  
379 (Gardner and others, 2019), to estimate the observed 2007–2018 ice fluxes at nine gates in the ablation  
380 area of Kaskawulsh Glacier. The flux gates (Figure 8a) are roughly perpendicular to the direction of ice  
381 flow, with five spanning the main trunk of the glacier and four spanning the major tributaries (North Arm,  
382 Central Arm, Stairway Glacier, South Arm). Ice-flux estimates are confined to the ablation area by the  
383 radar-data coverage. We compare the observed fluxes to balance fluxes at the same locations obtained using  
384 the modelled surface mass balance described above. Below we describe the determination of glacier cross-  
385 sectional area based on collection, processing and interpretation of ice-penetrating radar data, followed  
386 by the estimation of depth-averaged velocities using the NASA MEaSUREs ITS\_LIVE surface-velocity  
387 dataset.

## 388 **Flux-gate geometry**

### 389 *Ice-penetrating radar data collection*

390 Ground-based ice-penetrating radar (IPR) data were collected in 2018 and 2019 with a ruggedized BSI  
391 IceRadar system (Mingo and Flowers, 2010; Mingo and others, 2020), comprising a Narod and Clarke (1994)  
392 impulse transmitter (from Bennest Enterprises Ltd) with a  $\pm 600$  V pulse and a pulse repetition frequency  
393 (PRF) of 512 MHz. The receiving unit employs a 12-bit digitizer (Pico 4227), an integrated single-frequency  
394 global positioning system (GPS) unit (Garmin NMEA GPS18x) and BSI IceRadar Acquisition Software.  
395 The GPS unit is used only to obtain horizontal coordinates. Receiver and transmitter are connected to  
396 identical sets of resistively loaded dipole antennas of 5 MHz centre frequency which were towed in-line at  
397  $\sim 30$  m separation during the common-offset surveys. During data acquisition, we collected 1024 stacks every  
398 2–3 s at walking speed. The IPR surveys traversed debris-free and debris-covered ice, including some of the  
399 prominent medial moraines. Minor detours were required to navigate supraglacial streams, while data gaps  
400 within and at the ends of some transects arose from unnavigable terrain. In total,  $\sim 30$  line-km of data were  
401 collected.

### 402 *Ice-penetrating radar data processing and interpretation*

403 Gain control and band-pass filtering were applied to all radar data, following the processing workflow  
404 that we have established for ice-depth determination using this radar system in the same environmental  
405 setting (Wilson, 2012; Wilson and others, 2013; Bigelow, 2019; Bigelow and others, 2020). We tested  
406 two-dimensional frequency–wavenumber migration on all transects and considered results where migration  
407 did not introduce clearly implausible features. Two-way traveltimes were converted to depth considering  
408 receiver–transmitter separation and assuming a radar wave velocity of  $1.68 \times 10^8$  m s<sup>-1</sup> (Bogorodsky and  
409 others, 1985). The bed reflector was evident and unambiguous across most or all of the transect length  
410 for five of nine transects, while four of nine had larger areas of ambiguity. These areas were sometimes  
411 associated with the deepest ice (approaching  $\sim 1000$  m), and other times with clutter and/or scattering that  
412 would have obscured reflections.

413 In this study, uncertainty in ice depth arises from: (a) inherent uncertainty associated with signal  
414 wavelength, (b) the assumed radar velocity, (c) visibility and/or ambiguity of the bed reflector, (d) choices  
415 in data processing steps and (e) data gaps. Sources (c)–(e) are expected to dominate (a) and (b) in this  
416 study. To acknowledge these uncertainties, we identify minimum and maximum bounds on ice depth by  
417 producing a range of ice-depth profiles; we also produce a reference profile, which we subjectively deem

418 most plausible. The range of depth profiles arises from picking different reflectors, where they exist, to  
 419 address (c), considering migrated and unmigrated data to address (d) and employing linear versus non-  
 420 linear interpolation schemes to fill gaps between transect segments and between transect endpoints and  
 421 glacier margins to address (e). At least six and up to 12 different ice-depth profiles were generated for  
 422 each transect. The minimum, maximum and reference ice-depth profiles are shown in Figure 8. In order  
 423 of importance, the depth uncertainty imparted by (c) > (d) > (e), yet the sum of these uncertainties is a  
 424 minor contributor to ice-flux uncertainty.

### 425 **Depth-averaged velocities**

426 At each transect, cross-glacier depth-averaged velocity profiles (i.e.  $\bar{u}(y)$ ) are generated using surface-  
 427 velocity data and assumptions about flow partitioning between sliding and deformation. Surface velocities  
 428 are obtained from the NASA MEaSUREs Inter-Mission Time Series of Land Ice Velocity and Elevation  
 429 (ITS\_LIVE) project (Gardner and others, 2019). These data are generated using Landsat 4, 5, 7, and 8  
 430 imagery and auto-RIFT feature tracking (Gardner and others, 2018) to produce annual velocity mosaics. At  
 431 each of our flux gates, we extract annual surface velocity profiles from the 240 m × 240 m gridded ITS\_LIVE  
 432 dataset for the 2007–2018 study period.

From the 2007–2018 profiles we compute a 12-year mean velocity profile at each transect (Figure 8). We  
 consider three velocity models, which respectively give rise to lower, higher and intermediate estimates of  
 depth-averaged velocity  $\bar{u}$ : (a) all deformation ( $u_d$ ), no basal sliding ( $u_b$ ):  $\bar{u} = \bar{u}_d$ ,  $u_b = 0$ ; (b) all basal  
 sliding, no deformation (plug flow):  $\bar{u} = u_b$ ,  $u_d = 0$ ; and (c) some combination of deformation and basal  
 sliding:  $\bar{u} = \bar{u}_d + u_b$ . In (a) we take  $\bar{u}_d = 0.8 u_s$ , where  $u_s$  is the surface velocity (Nye, 1965), thus  $\bar{u} = 0.8 u_s$ .  
 In (b)  $\bar{u} = u_s$ . In (c), we estimate the contribution of deformation to surface velocity using the shallow ice  
 approximation, up to a maximum of the observed surface velocity:

$$u_d(z = s) = \max \left( u_s, \frac{2A}{n+1} (\rho_i g \sin \theta)^n h^{n+1} \right), \quad (8)$$

433 with  $A = 2.4 \times 10^{-24} \text{ Pa}^{-3} \text{ s}^{-1}$  the assumed value of the flow-law coefficient for temperate ice (Cuffey and  
 434 Paterson, 2010),  $n = 3$  the flow-law exponent,  $\rho_i = 910 \text{ kg m}^{-3}$  the density of ice,  $g = 9.81 \text{ m s}^{-2}$  the  
 435 acceleration due to gravity,  $h$  the ice depth and  $\theta$  the glacier surface slope. For each transect, we estimate  
 436  $\theta$  as the width-averaged surface slope in the downflow direction based on the TanDEM-X DEM.

437 Any underestimation of the observed surface velocity by the value calculated in Equation 8 is attributed  
 438 to basal sliding:  $u_b = u_s - u_d(z = s)$ . The depth-averaged velocity is then  $\bar{u} = 0.8 u_d(z = s) + u_b$  or

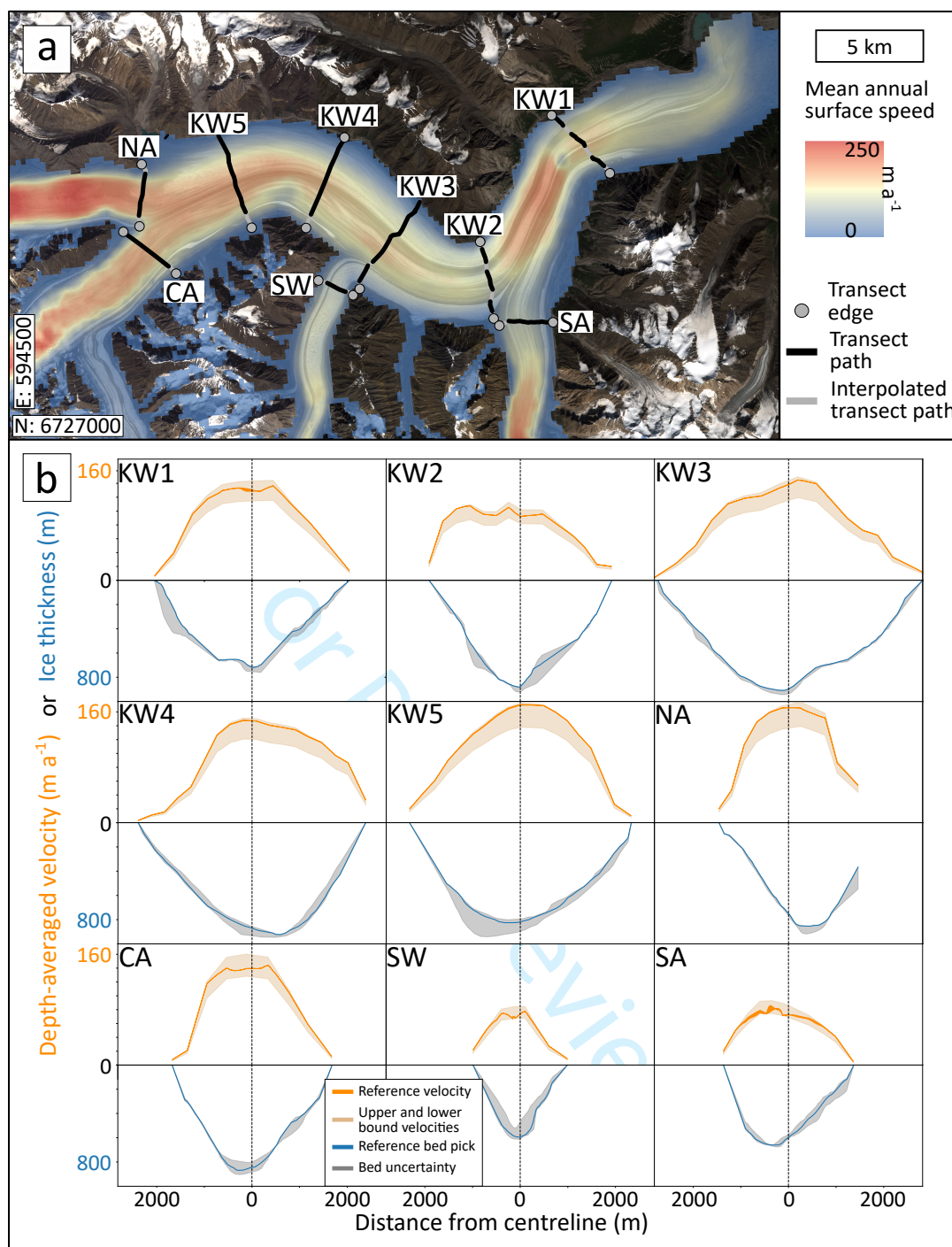


**Fig. 8.** Observed profiles of ice thickness and depth-averaged velocity. (a) Kaskawulsh Glacier ablation zone with locations of radar transects across the main trunk (KW1–KW5) and across confluences with major tributaries: North Arm (NA), Central Arm (CA), South Arm (SA), Stairway Glacier (SW). Mean 2007–2018 surface velocity is shown in colour. Velocity data generated using auto-RIFT (Gardner and others, 2018) and provided by the NASA MEaSURES ITS\_LIVE project (Gardner and others, 2019). UTM (Zone 7 North) coordinates of southwest corner: 594500 E, 6727000 N. Copernicus Sentinel data 2017. Retrieved from Copernicus Open Access Hub 01/11/17. (b) Depth-averaged velocity profiles with uncertainty (orange) and ice-thickness profiles with uncertainty (blue) at each transect.

**Table 3.** Measured cross-sectional area  $A_{xc}$  and ice discharge  $Q$  at flux gates.  $Q$  ( $\text{km}^3 \text{a}^{-1}$ ) is derived from cross-sectional area and ITS\_LIVE surface velocities for three different velocity–depth profiles: (1) all deformation, no sliding:  $\bar{u} = \bar{u}_d$ ,  $u_b = 0$  ( $Q_{\text{low}}$ ); (2) all sliding, no deformation (plug flow):  $\bar{u} = u_b$ ,  $u_d = 0$  ( $Q_{\text{high}}$ ); (3) deformation and sliding combined:  $\bar{u} = \bar{u}_d + u_b$  ( $Q_{\text{ref}}$ ). Tributary flux gates are: North Arm (NA), Central Arm (CA), Stairway Glacier (SW), South Arm (SA). Flux gates along the main trunk are: KW5 (highest) to KW1 (lowest).  $\pm$  indicates one standard deviation arising from bed interpretation for  $A_{xc}$  and variations in bed interpretation only for the fluxes. Bold values are explained in text.

Flux gate	$A_{xc}$ ( $\text{km}^2$ )	$\pm$	$Q_{\text{low}}$ ( $\text{km}^3 \text{a}^{-1}$ )	$\pm$	$Q_{\text{high}}$ ( $\text{km}^3 \text{a}^{-1}$ )	$\pm$	$Q_{\text{ref}}$ ( $\text{km}^3 \text{a}^{-1}$ )	$\pm$
NA	1.60	0.06	<b>0.182</b>	0.005	0.227	0.007	0.221	0.006
CA	1.80	0.07	0.180	0.007	0.225	0.009	<b>0.209</b>	0.006
SW	0.66	0.09	0.036	0.004	<b>0.045</b>	0.006	0.042	0.004
SA	1.14	0.07	0.069	0.003	<b>0.086</b>	0.004	0.075	0.002
KW5	2.57	0.15	0.275	0.015	0.344	0.018	<b>0.341</b>	0.017
KW4	2.96	0.14	<b>0.265</b>	0.008	0.331	0.011	0.326	0.010
KW3	3.12	0.08	<b>0.266</b>	0.005	0.333	0.006	0.326	0.006
KW2	1.97	0.11	0.144	0.008	<b>0.181</b>	0.010	0.174	0.008
KW1	1.72	0.09	<b>0.164</b>	0.005	0.205	0.007	0.195	0.005

439  $\bar{u} = u_s - 0.2 u_d(z = s)$ . The choice of velocity model is the leading source of uncertainty in the ice-flux  
 440 calculations.

#### 441 Observed ice fluxes

442 Ice-flux (in units of  $\text{km}^3 \text{a}^{-1}$ ) is calculated at each flux gate (i.e. transect) by numerically integrating the  
 443 product of ice depth (derived from radar data) and depth-averaged velocity (derived from ITS\_LIVE data)  
 444 across the transect (i.e. glacier width). This calculation is done for each of the 6–12 ice-depth profiles  
 445 per transect and each of the three depth-averaged velocity models above, yielding 18–36 values of ice  
 446 flux per transect. The reference flux at each transect employs the reference ice-depth profile, and the  
 447 intermediate velocity model (c), where the shallow-ice approximation is used to estimate the contribution  
 448 of deformation to the surface velocity (Equation 8) and the remainder is attributed to sliding. We assign  
 449 an uncertainty on each ice flux in Table 3 ( $Q_{\text{low}}$ ,  $Q_{\text{high}}$ ,  $Q_{\text{ref}}$ ) equal to the standard deviation of the 6–12  
 450 values. This uncertainty represents only that arising from bed interpretation, whereas the range of  $Q_{\text{low}}$  to  
 451  $Q_{\text{high}}$  encompasses the uncertainty arising from different velocity models.

452 **ANALYSIS AND INTERPRETATION**453 **Comparison of modelled and inferred mass-balance distribution**

Using the surface elevation change of the Kaskawulsh Glacier (Figure 2), the ice fluxes at each of nine flux gates (Figure 8) and the modelled surface mass balance (Figure 7), we are able to independently estimate each term in the continuity equation:

$$\frac{\partial h}{\partial t} + \nabla \cdot q = \dot{b}_{\text{sfc}}, \quad (9)$$

454 where  $\partial h/\partial t$  is the local rate of change of ice thickness,  $\nabla \cdot q$  is the divergence of the flux and  $\dot{b}_{\text{sfc}}$  is the surface  
 455 mass balance (with density adjustments for m w.e. a<sup>-1</sup> of 850 kg m<sup>-3</sup> and 900 kg m<sup>-3</sup> applied to  $\partial h/\partial t$  and  
 456  $\nabla \cdot q$ , respectively). In order to assess the consistency of our remotely sensed elevation changes, measured  
 457 ice fluxes and modelled mass balance, we compare each independently estimated term in the continuity  
 458 equation to its counterpart calculated using the other terms, for each section of the glacier bounded by flux  
 459 gates and the ice margin.

460 We then compute the RMSE between the two estimates of each term for each section of the glacier for  
 461 both debris-free and debris-present cases of the mass-balance model. Inspection of the RMSEs reveals that  
 462 the debris-present case outperforms the debris-free case for each term in the continuity equation: 1.43 vs  
 463 1.61 m w.e. a<sup>-1</sup> for  $\partial h/\partial t$ , 0.064 vs 0.077 km<sup>3</sup> w.e. a<sup>-1</sup> for  $\nabla \cdot q$  and 1.31 vs 1.47 m w.e. a<sup>-1</sup> for  $\dot{B}_{\text{sfc}}$ . The  
 464 debris-present case also outperforms the debris-free case using mean error rather than RMSE as a metric.  
 465 We therefore consider  $\dot{b}_{\text{sfc}}$  obtained with the debris-present model to be the reference mass-balance field  
 466 in the following analysis. Although the spatial pattern associated with debris-covered medial moraines in  
 467 the mass-balance model (Figure 7b) is not clearly reflected in the observed surface lowering (Figure 2),  
 468 the superior performance of the model with debris is nevertheless unsurprising: muted thinning rates over  
 469 the lowermost ~5 km of the glacier (Figure 2) do coincide with extensive debris cover. Furthermore, the  
 470 ablation suppressed by debris in the model is compensated by enhanced ablation over debris-free ice owing  
 471 to the requirement (in Stage 1 tuning) that modelled glacier-wide mass balance match the geodetic balance  
 472 within uncertainty; the resulting model parameters ( $MF$ ,  $a_{\text{snow/ice}}$ ) for the debris-present case yield a lower  
 473 modelled mass-balance gradient, which is in better agreement with the observations. A similar dependence  
 474 of the mass-balance gradient on debris cover has been observed on glaciers in High Mountain Asia (Bisset  
 475 and others, 2020).

476 By using ice-thickness data collected in 2018–2019, we systematically underestimate 2007–2018 mean  
 477 ice fluxes due to thinning during the study period. In order to assess the maximum impact of this



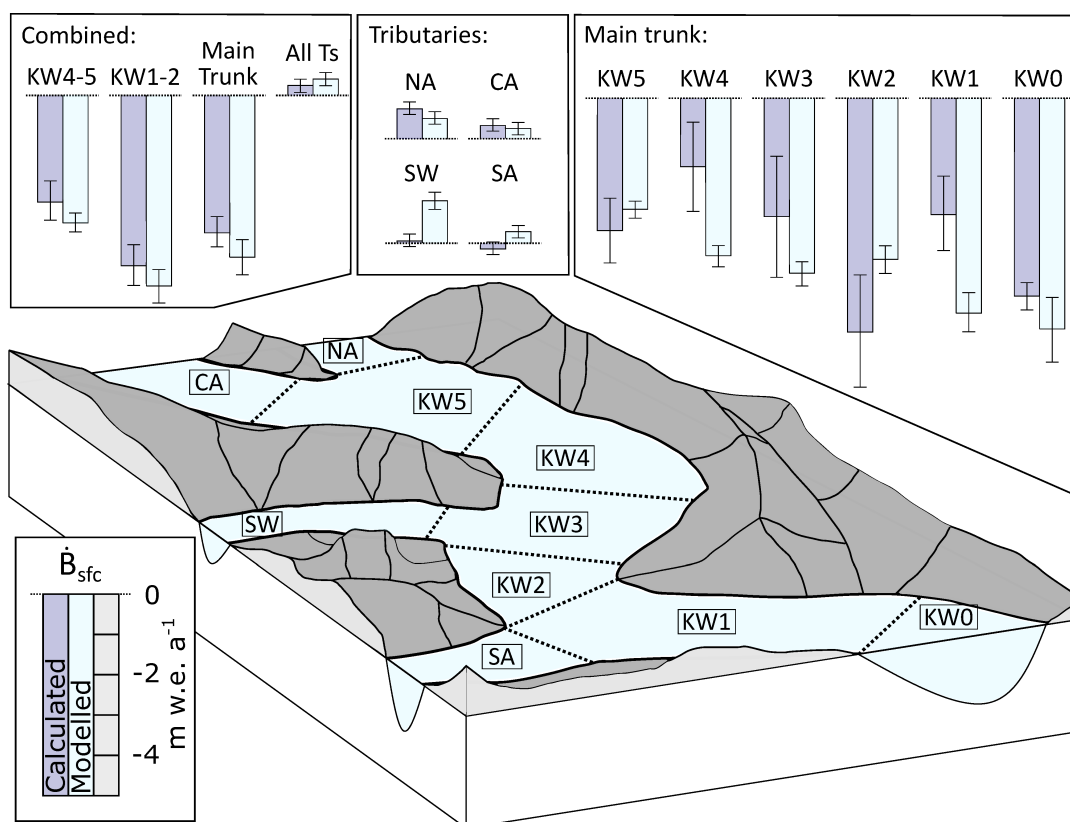


**Fig. 9.** Comparison of calculated ( $\dot{B}_{\text{cal}}$ , light purple) and modelled ( $\dot{B}_{\text{mod}}$ , light blue) mass balance, with associated uncertainties, for each section of the glacier. Sections are labelled according to their downstream flux gates. Also shown are four combined sections: KW4+KW5, KW1+KW2, KW0–KW5 (“Main trunk”) and NA+CA+SW+SA (“All Ts” (all tributaries)).

478 underestimation on  $\nabla \cdot q_{\text{obs}}$ , we use the observed elevation change (data in Figure 2) to calculate total  
 479 thinning at each flux gate between 2007 and 2018. Note that gap-filled areas comprise up to 53% (KW2) of  
 480 the length of individual flux gates. This calculation yields an average change in  $\nabla \cdot q_{\text{obs}}$  of  $\sim 1.5 \pm 1.2\%$ , with  
 481 the greatest change between KW4 and KW5 ( $\sim 4\%$ ) and least between KW1–KW2 ( $< 1\%$ ). These values  
 482 reflect flux changes over the entire study period, and are thus twice what might be considered representative  
 483 of the 2007–2018 mean.

484 Below we focus on the comparison between modelled ( $\dot{B}_{\text{mod}}$ ) and calculated ( $\dot{B}_{\text{cal}}$ ) mass balance for each  
 485 section of the glacier bounded by flux gates and the glacier margin, where  $\dot{B}_{\text{mod}}$  is the integral of  $\dot{b}_{\text{sfc}}$   
 486 between the flux gates of interest and  $\dot{b}_{\text{sfc}}$  is obtained directly from the mass-balance model with debris.  
 487  $\dot{B}_{\text{cal}}$  is obtained by summing the elevation change ( $\partial h / \partial t$ ) over the section of interest and the difference in  
 488 measured downstream and upstream fluxes ( $\nabla \cdot q$ ) (Equation 9). This comparison is one means of evaluating  
 489 the mass-balance model, but also reveals potential shortcomings in the other derived quantities.

**Table 4.** Independently estimated (subscript “obs” or “mod”) versus calculated (subscript “cal”) terms in the continuity equation (Equation 9) for each section of the glacier (labelled with downstream flux gate as in Figure 9):  $\frac{\partial h}{\partial t}_{\text{cal}} = -\nabla \cdot q_{\text{obs}} + \dot{B}_{\text{mod}}$ ,  $\dot{B}_{\text{cal}} = \frac{\partial h}{\partial t}_{\text{obs}} + \nabla \cdot q_{\text{obs}}$ ,  $\nabla \cdot q_{\text{cal}} = \dot{B}_{\text{mod}} - \frac{\partial h}{\partial t}_{\text{obs}}$ . Values of  $\nabla \cdot q$  are converted to m w.e. a<sup>-1</sup> using an ice density of 900 kg m<sup>-3</sup>.

Flux Gate(s)	Surface Area km <sup>2</sup>	Gap fill %	$\frac{\partial h}{\partial t}_{\text{obs}}$ m w.e. a <sup>-1</sup>	$\frac{\partial h}{\partial t}_{\text{cal}}$ m w.e. a <sup>-1</sup>	$\nabla \cdot q_{\text{obs}}$ m w.e. a <sup>-1</sup>	$\nabla \cdot q_{\text{cal}}$ m w.e. a <sup>-1</sup>	$\dot{B}_{\text{mod}}$ m w.e. a <sup>-1</sup>	$\dot{B}_{\text{cal}}$ m w.e. a <sup>-1</sup>
NA	218	38	-0.18	-0.41	0.91	0.67	0.50	0.74
CA	319	17	-0.28	-0.34	0.59	0.53	0.25	0.31
SW	107	16	-0.32	0.68	0.35	1.36	1.04	0.03
SA	262	37	-0.40	0.02	0.26	0.68	0.28	-0.14
KW5	32	8	-0.80	-0.23	-2.47	-1.90	-2.70	-3.28
KW4	22	15	-1.07	-3.22	-0.62	-2.77	-3.84	-1.69
KW3	22	45	-1.21	-2.53	-1.73	-3.05	-4.26	-2.93
KW2	29	49	-1.17	0.72	-4.64	-2.75	-3.92	-5.81
KW1	36	12	-1.53	-3.87	-1.37	-3.71	-5.23	-2.89
KW0	48	21	-1.55	-2.35	-3.27	-4.07	-5.62	-4.82
KW1+KW2	65	28	-1.37	-1.79	-2.85	-3.27	-4.64	-4.22
KW4+KW5	54	11	-0.91	-1.43	-1.73	-2.25	-3.16	-2.64
All tributaries	907	28	-0.29	-0.13	0.54	0.71	0.41	0.25
Main trunk	189	24	-1.17	-1.76	-2.25	-2.85	-4.01	-3.41
Glacier-wide	1096	28	-0.46	-0.42	0.00	0.04	-0.42	-0.46

#### 490 Sections upstream of tributary flux gates

491 Values of  $\dot{B}_{\text{mod}}$  are positive for all four tributaries (NA, CA, SW, SA in Figure 9) but underestimate  $\dot{B}_{\text{cal}}$  for  
 492 North and Central Arms, while overestimating  $\dot{B}_{\text{cal}}$  for Stairway Glacier and South Arm.  $\dot{B}_{\text{cal}}$  for Stairway  
 493 Glacier (the smallest of the four catchments) is near-zero and for South Arm is negative.  $\dot{B}_{\text{mod}}$  and  $\dot{B}_{\text{cal}}$   
 494 agree within uncertainty only for the North and Central Arms. Averaged across all four tributaries,  $B_{\text{mod}}$   
 495 exceeds  $B_{\text{cal}}$  by 0.16 m w.e.

496 The differences between  $\dot{B}_{\text{mod}}$  and  $\dot{B}_{\text{cal}}$  hint that spatial variability in the accumulation field not captured  
 497 by the model might play an important role in explaining this mismatch, and in Kaskawulsh Glacier mass  
 498 balance. The better agreement between  $\dot{B}_{\text{mod}}$  and  $\dot{B}_{\text{cal}}$  in the North and Central Arms is unsurprising given  
 499 the provenance of the high-elevation measurements used in the accumulation bias correction (Figure 5). A  
 500 strong roughly east–west moisture gradient exists in the region due to the orographic divide of the St. Elias

501 Mountains: applying a bias correction exclusively based on elevation and without data from the southern  
 502 half of the catchment (the accumulation areas of Stairway Glacier and South Arm) would not account for  
 503 geographic differences in accumulation. Given that Stairway Glacier and South Arm are further from the  
 504 orographic divide, we suspect the accumulation bias correction—based on high-elevation data restricted to  
 505 the western margin of the catchment—leads to overestimation of modelled mass balance in these southern  
 506 tributary catchments. The North and Central Arms also differ from Stairway Glacier and South Arm in  
 507 aspect, with the former being eastern to north-eastern and the latter being northern. Aspect plays a direct  
 508 role in modelled ablation through parameters  $a_{\text{snow/ice}}$ , while the orientation of mountain ridges relative to  
 509 the prevailing wind would also play a role in snow redistribution, a process unaccounted for in the model.

### 510 *Sections downstream of the tributary flux gates*

511 Within the main trunk of the glacier, we compare  $\dot{B}_{\text{mod}}$  and  $\dot{B}_{\text{cal}}$  for six sections bounded by the flux  
 512 gates and the glacier margin/terminus. The differences between  $\dot{B}_{\text{mod}}$  and  $\dot{B}_{\text{cal}}$  are large and their signs  
 513 inconsistent (Figure 9):  $\dot{B}_{\text{mod}}$  exceeds  $\dot{B}_{\text{cal}}$  by 2.15, 1.33, 2.34 and 0.80 m w.e. (127%, 45%, 79% and 17%)  
 514 for sections upstream of KW4, KW3, KW1 and the terminus, respectively, while  $\dot{B}_{\text{cal}}$  exceeds  $\dot{B}_{\text{mod}}$  by  
 515 0.58 m w.e. and 1.89 m w.e. (21% and 49%) upstream of KW5 and KW2, respectively.  $\dot{B}_{\text{mod}}$  and  $\dot{B}_{\text{cal}}$  only  
 516 agree within uncertainty for three of six sections. Notably, in the lowermost section between KW1 and the  
 517 terminus (labelled KW0) where the debris coverage is highest, the debris-present model far outperforms the  
 518 debris-free model, yielding  $\dot{B}_{\text{mod}} = -5.62 \pm 0.46$  m w.e. versus  $-9.64 \pm 0.99$  m w.e. for the debris-free model,  
 519 compared to  $\dot{B}_{\text{cal}} = -4.82 \pm 0.16$  m w.e. The magnitude of this difference is in line with the reduction of  
 520 ablation by terminus debris cover observed in High Mountain Asia (e.g. Vincent and others, 2016; Bisset  
 521 and others, 2020).

522 Visual inspection of Figure 9 reveals changes in the sign of the mismatch between  $\dot{B}_{\text{mod}}$  and  $\dot{B}_{\text{cal}}$  in some  
 523 adjacent sections of the glacier, suggesting that mismatch could be reduced by combining these sections.  
 524 For example, if we combine sections KW4 and KW5,  $\dot{B}_{\text{mod}}$  and  $\dot{B}_{\text{cal}}$  differ by only 22% (Figure 9, Table 4).  
 525 Similarly, KW1 and KW2 together reduce the mismatch between  $\dot{B}_{\text{mod}}$  and  $\dot{B}_{\text{cal}}$  to 11%. Considering the  
 526 entire region below the tributary fluxgates,  $\dot{B}_{\text{mod}}$  is more negative than  $\dot{B}_{\text{cal}}$  ( $-4.01$  versus  $-3.41$  m w.e.),  
 527 whereas above the tributary flux gates  $\dot{B}_{\text{mod}}$  is more positive ( $0.41$  versus  $0.25$  m w.e.) (Figure 9, Table 4).  
 528 The modelled mass-balance gradient is therefore steeper than that inferred from  $\partial h/\partial t + \nabla \cdot q$ .

529 Missing physical processes can also explain some of the mismatch between  $\dot{B}_{\text{mod}}$  and  $\dot{B}_{\text{cal}}$ . For example,  
 530 the section above KW5 is influenced by the presence of an ice-marginal lake with a calving front (Bigelow

531 and others, 2020), which results in additional mass loss. This loss is not accounted for in the mass-balance  
 532 model, but nevertheless influences changes in surface elevation and ice flux. Though unquantified, the  
 533 anticipated mass loss into the lake basin is consistent with the sign of the mismatch between  $\dot{B}_{\text{mod}}$  and  $\dot{B}_{\text{cal}}$   
 534 above the KW5 flux gate.

535 Discrepancies between  $\dot{B}_{\text{mod}}$  and  $\dot{B}_{\text{cal}}$  can also be due to observational errors or uncertainty that influence  
 536  $\dot{B}_{\text{cal}}$ , in addition to shortcomings of the mass-balance model. Occurrence of cloud cover or the presence of  
 537 regions where stereo-image texture is too homogeneous creates the need to gap-fill the observed elevation-  
 538 change field ( $\partial h/\partial t$  in Equation 9). These gaps could contribute to mismatch between  $\partial h/\partial t_{\text{cal}}$  and  $\partial h/\partial t_{\text{obs}}$ :  
 539 27.7% of the total glacier area is gap-filled (Figure 2), with a local maximum of 48.7% for the section  
 540 upstream of KW2 (Table 4). Because the gap-filling scheme is a function of elevation only, it does not  
 541 capture small-scale spatial variability associated with debris cover, aspect or geographical location within  
 542 the catchment (McNabb and others, 2019). This is problematic at higher elevations, which cover a wide  
 543 geographical range with variable aspects. Compounded with larger relative errors at high elevation (owing  
 544 to smaller values of elevation change), we expect the gap-filled values at high elevations may be less  
 545 representative of local conditions.

546 Errors also arise in the calculation of ice fluxes. There are three major sources of uncertainty in our  
 547 calculation: that associated with (1) ice depth, due to processing and interpretation of the radar data, (2)  
 548 surface velocity, arising from inter-annual variability evident in the ITS\_LIVE data and (3) the velocity-  
 549 depth profile, owing to the unknown partitioning of surface velocity between deformation and sliding. The  
 550 latter is the largest. Inconsistency also arises from using radar data collected in 2018–2019 to compute  
 551 2007–2018 fluxes, given the nearly pervasive thinning observed from 2007–2018 (Figure 2).

552 Entertaining the possibility that  $Q_{\text{ref}}$  (Table 3) may not be the correct representation of flux at each gate,  
 553 we explore the impact of substituting  $Q_{\text{low}} \pm \sigma$  (no sliding) and  $Q_{\text{high}} \pm \sigma$  (plug flow) for  $Q_{\text{ref}}$ . By increasing  
 554 the sliding contribution at gates SW, SA and KW2, and decreasing it at gates NA, KW4, KW3 and KW1  
 555 (see bold values in Table 3), we reduce metrics of overall mismatch between  $\nabla \cdot q_{\text{obs}}$  and  $\nabla \cdot q_{\text{cal}}$  (Table  
 556 4) by  $\sim 20$ – $40\%$  and section-wise mismatch of  $\nabla \cdot q_{\text{obs}}$  and  $\nabla \cdot q_{\text{cal}}$  downstream of the tributary flux gates  
 557 from  $>75\%$  to  $<25\%$  (not shown). The resulting mismatch between  $\dot{B}_{\text{cal}}$  and  $\dot{B}_{\text{mod}}$  is more systematic and  
 558 spatially coherent than that using  $Q_{\text{ref}}$  in Figure 9, particularly below the tributary flux gates (not shown).  
 559 With one minor exception,  $\dot{B}_{\text{cal}}$  underestimates the magnitude of  $\dot{B}_{\text{mod}}$  by 11–24% for KW0–KW5 ( $\dot{B}_{\text{cal}}$   
 560 overestimates the magnitude of  $\dot{B}_{\text{mod}}$  by 9% for KW4). Although it would be circular to tune  $\dot{B}_{\text{cal}}$  to  $\dot{B}_{\text{mod}}$

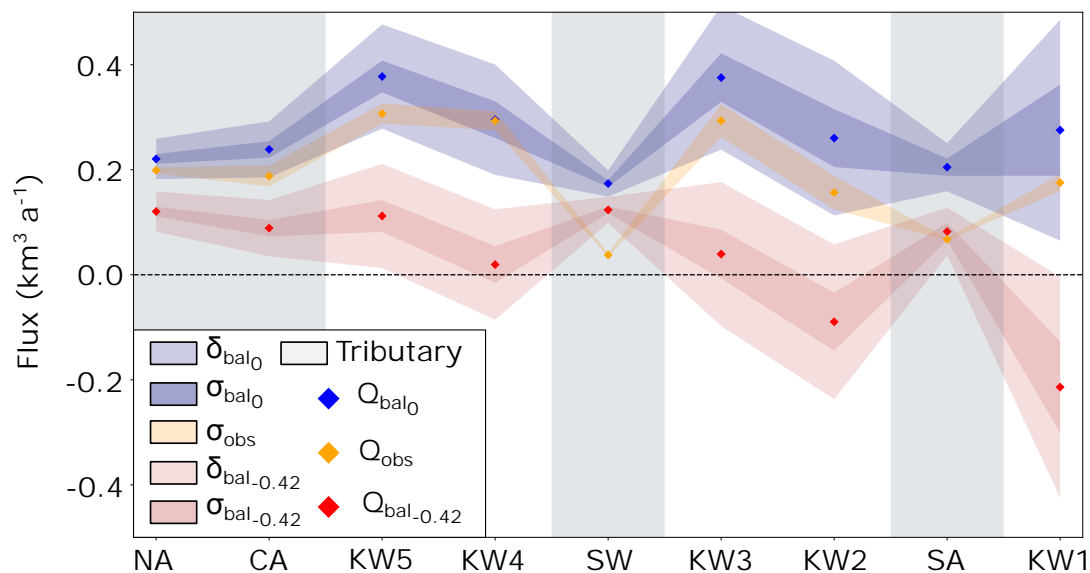


**Fig. 10.** Comparison of observed and balance fluxes arranged according to position of flux gate (tributaries shaded in grey). See Figure 8 for flux-gate locations. Observed fluxes ( $Q_{obs}$ , yellow) are shown with standard deviations arising only from glacier-bed interpretation (see  $Q_{ref}$  in Table 3). Balance fluxes are shown for  $\dot{B}_{sfc} = 0$  ( $Q_{bal0}$ , blue) and  $\dot{B}_{sfc} = -0.42$  m w.e. ( $Q_{bal-0.42}$ , red). Dark red/blue shading is standard deviation of balance fluxes for the 12 simulations that satisfy both stages of model tuning for debris-present case. Light red/blue shading is the uncertainty for each balance flux determined from the uncertainties on model accumulation and melt rates. Shading is continuous between flux gates only to assist in visual interpretation; not all flux gates are connected as suggested by shading.

561 by changing the fluxes, this exercise demonstrates that it is possible to satisfy the local continuity equation  
 562 simply by exploring plausible variations in glacier dynamics via the partitioning of sliding and deformation.  
 563 It also corroborates our finding that the modelled mass-balance gradient is steeper than that inferred from  
 564  $\partial h / \partial t + \nabla \cdot q$ .

### 565 Comparison of balance fluxes and observed fluxes

566 We compare our model-derived balance fluxes ( $Q_{bal}$ ) and observed fluxes ( $Q_{obs}$ ) at each flux gate  
 567 to investigate the inconsistency between internal mass redistribution and surface mass balance of the  
 568 Kaskawulsh Glacier (Figure 10). First, we determine two sets of balance fluxes: (1) those derived from  
 569 the 2007–2018 modelled mass balance where  $\dot{B}_{sfc} = -0.42$  m w.e. a<sup>-1</sup> (denoted  $Q_{bal-0.42}$ ), and (2) those  
 570 adjusted to balance conditions ( $\dot{B}_{sfc} = 0$ ) (Azam and others, 2012) by adding  $-0.42$  m w.e. a<sup>-1</sup> to the  $b_{sfc}$   
 571 field (denoted  $Q_{bal0}$ ). The contrast between these balance fluxes is used to situate the current state of  
 572 response of the observed ice fluxes to a changing surface mass balance.

573 With the exception of the SW and SA flux gates, where the balance fluxes are impacted by the suspected  
574 overestimation of modelled accumulation, the spatial structure of  $Q_{\text{obs}}$  resembles that of  $Q_{\text{bal}_0}$  (Figure 10).  
575 The magnitudes of  $Q_{\text{obs}}$  are lower than those of  $Q_{\text{bal}_0}$ , but significantly higher than those of  $Q_{\text{bal}_{-0.42}}$ . The  
576 similarity in distribution and magnitude of  $Q_{\text{obs}}$  and  $Q_{\text{bal}_0}$  indicates that the glacier flow regime more closely  
577 reflects zero balance conditions than the negative balance conditions of 2007–2018, and thus the dynamic  
578 adjustment of the glacier is far from complete. This state of adjustment demonstrates that the response  
579 time of the Kaskawulsh Glacier exceeds the  $\sim 40$  years over which mass-balance conditions similar to those  
580 of 2007–2018 have persisted (Berthier and others, 2010), as expected for a glacier of this size and in this  
581 climate (Cuffey and Paterson, 2010).

582 The balance flux  $Q_{\text{bal}_{-0.42}}$  becomes negative between gates KW3 and KW2 (Figure 10). Owing to the  
583 suspected overestimation of accumulation in the SW and SA tributaries, which feed downstream gates KW3  
584 and KW1, respectively, the spatial extent of negative balance fluxes is likely a conservative estimate. In order  
585 to more precisely determine the position of zero balance flux ( $KW_{\text{null}}$ ), we discretize the region between  
586 KW3 and KW2 into numerous flux gates and integrate the modelled surface mass balance upstream of  
587 each one. We estimate  $KW_{\text{null}}$  to be  $23.2 \pm 3.2$  km upstream of the current terminus position, and upstream  
588 of the South Arm confluence, at an elevation of 1447 m a.s.l (Figure 1). This position suggests the main  
589 trunk of the Kaskawulsh Glacier would detach from the South Arm under sustained conditions of 2007–2018  
590 mass balance. Using a slightly adjusted (Langhammer and others, 2019) version of the Farinotti and others  
591 (2019) ensemble estimate of glacier bed topography, we estimate that  $46 \text{ km}^3$  of ice, or  $\sim 15\%$  of the total  
592 Kaskawulsh Glacier volume, reside in the main trunk of the glacier below the position of zero balance flux.  
593 Given that our calculation ignores flow across the line of zero balance as well as upstream thinning, this  
594 volume is a minimum bound on the committed ice loss (Mernild and others, 2013) if the 2007–2018 climate  
595 persists. Considering the projected increase of global and regional air temperatures (Allen and others, 2014)  
596 compared to our model inputs, the negative mass-balance conditions that characterized 2007–2018 will likely  
597 be exacerbated in the future and drive the position of zero balance flux even further up-glacier.

## 598 DISCUSSION

599 The rate of mass loss we estimate for 2007–2018 ( $-0.46 \pm 0.17 \text{ m w.e. a}^{-1}$ ) is higher than that estimated by  
600 Larsen and others (2015) for 1995–2013 ( $-0.35 \text{ m w.e. a}^{-1}$ ), the only other glacier-wide study. Our 2007–2018  
601 estimate is, however, indistinguishable from that of Berthier and others (2010), both for the Kaskawulsh  
602 Glacier individually ( $-0.46 \pm 0.20 \text{ m w.e. a}^{-1}$ , 1977–2007) and the entire glacier population of the St. Elias

603 Mountains ( $-0.47 \pm 0.09$  m w.e.  $\text{a}^{-1}$ , 1968–2006). While mass loss may have accelerated from 1995–2018, we  
604 cannot conclude that it accelerated in the last decade (2007–2018) relative to the four before (1968–2006).

605 Mass loss occurs in two modes for land-terminating glaciers (e.g. Thomson and others, 2017): (1) ice  
606 fluxes in excess of balance fluxes move mass to lower ablation-prone areas causing upstream thinning (and  
607 an attendant reduction in driving stress) without significant terminus retreat, and (2) reduced ice fluxes lead  
608 to accelerated thinning in the mass-starved ablation-prone areas (e.g. Span and Kuhn, 2003) and eventually  
609 to glacier retreat. Previous work on small alpine glaciers ( $\leq 30$  km<sup>2</sup>) has documented significantly reduced  
610 ice fluxes and accelerated thinning within a decade of decreasing surface mass balance (e.g. Azam and  
611 others, 2012; Berthier and Vincent, 2012; Dehecq and others, 2019). This ice-flux reduction can overshoot  
612 the mass balance forcing even for very small glaciers, resulting in balance fluxes greater than observed  
613 fluxes (Meier and Tangborn, 1965). The dynamic response can be further complicated by frontal ablation  
614 for marine terminating glaciers (Deschamps-Berger and others, 2019), variation in surface debris (e.g. Benn  
615 and others, 2012; Bhattacharya and others, 2016) and glacier geometry (encompassing area/volume, and  
616 hypsometry) (e.g. Chinn, 1999). The fact that observed fluxes for the Kaskawulsh Glacier ( $Q_{\text{obs}}$ ) are more in  
617 line with balance fluxes adjusted to zero-balance conditions ( $Q_{\text{bal}_0}$  vs  $Q_{\text{bal}_{-0.42}}$ ) suggests that driving stresses  
618 have not diminished appreciably (this is further corroborated by a lack of systematic surface velocity drop  
619 between 2007–2018 (See Supplementary Material). This situation is consistent with mode 1 (see above)  
620 mass loss for the Kaskawulsh Glacier.

621 Based on the position of the zero balance flux ( $Q_{\text{bal}_{-0.42}} = 0$ ), we calculate a minimum of  $\sim 23$  km of  
622 committed glacier retreat if the 2007–2018 climate were to hold steady. Although we cannot assign a  
623 timescale to this retreat, Foy and others (2011) have determined a rate of terminus retreat of  $\sim 13$  m  $\text{a}^{-1}$   
624 (derived from terminus tracking between 1956–2007 using aerial and satellite imagery) that increased  
625 between 2000 and 2007. Reyes and others (2006) estimate a late Holocene retreat rate of  $\sim 80$ – $100$  m  $\text{a}^{-1}$   
626 based on dendroglaciological studies of the Little Ice Age (LIA) maximum. Due to the onset of Kaskawulsh  
627 retreat occurring later than the regional LIA maximum (early- to mid-18th century), the estimated retreat  
628 rate is likely conservative (Borns and Goldthwait, 1966; Reyes and others, 2006). At these historically  
629 estimated rates, the committed retreat of  $\sim 23$  km would occur on timescales of a century or longer.

630 Our observations of glacier mass loss coincide with an observed multi-decadal increase in regional air  
631 temperature (Streicker, 2016) that is projected to continue for decades to come. Yukon has experienced  
632 a greater warming rate than most regions in Canada: a  $2.4^\circ\text{C}$  increase in mean annual air temperature

633 for 1948–2016 (ECCC, 2019b) compared to  $\sim 1.7^{\circ}\text{C}$  for the entire country (ECCC, 2019b). Relative to the  
634 1980–2000 mean, an additional  $2.1\text{--}3.3^{\circ}\text{C}$  warming is expected for Yukon by mid-century (2040–2060) and  
635  $2.2\text{--}6.4^{\circ}\text{C}$  by late-century (2080–2100) (Data from Environment and Climate Change Canada) based on  
636 Representative Concentration Pathways (RCPs) 2.6 and 8.5, respectively, from the Fifth Assessment Report  
637 of Intergovernmental Panel of Climate Change (IPCC). Winter temperature increase is typically double the  
638 annual mean (Streicker, 2016; ECCC, 2019a). Total annual precipitation in Yukon has increased by 6%  
639 between 1964–2014 (Streicker, 2016), with a 12–15% increase projected for mid-century (2040–2060) and  
640 12–35% for late-century (2080–2100) relative to the 1980–2000 mean (Data from Environment and Climate  
641 Change Canada), less than has been estimated elsewhere to offset the effects of warming (e.g. De Woul and  
642 Hock, 2005). With the anticipated warming yet to come by 2100, the glacier mass-loss rate and committed  
643 retreat we have estimated based on 2007–2018 data are lower than should be expected for mid- to late-21st  
644 century climate conditions.

## 645 CONCLUSION

646 This work is the first attempt, to our knowledge, to investigate the mass budget of a large land-terminating  
647 glacier extending  $\sim 70$  km over  $\sim 2500$  m of elevation, using direct measurements of ice geometry and fully  
648 distributed mass-balance modelling. We have combined new measurements of surface-elevation change,  
649 observed ice fluxes and modelled surface mass balance to calculate the mass budget of the Kaskawulsh  
650 Glacier. We estimate a 2007–2018 geodetic balance of  $-0.46 \pm 0.17$  m w.e.  $\text{a}^{-1}$ , comparable to the 1977–  
651 2007 estimate for the Kaskawulsh Glacier and the 1968–2006 estimate for the wider region. The rate of  
652 mass loss and associated glacier thinning is expected to accelerate with continued warming. In comparing  
653 observed ice fluxes to model-derived balance fluxes we estimate a committed terminus retreat of  $23.2 \pm 3.2$  km  
654 and a lower bound of  $46 \text{ km}^3$  of ice loss, corresponding to  $\sim 15\%$  of the total glacier volume. This retreat  
655 will result in fragmentation of the Kaskawulsh Glacier, with the main trunk retreating past the confluence  
656 with the South Arm. We find that measured ice fluxes are closer to balance fluxes adjusted to zero-balance  
657 conditions than to 2007–2018 balance fluxes, indicating that the glacier is still in the early stages of dynamic  
658 adjustment to mass imbalance.

659 By analyzing discrepancies between modelled, observed and derived quantities in the context of the  
660 continuity equation, we have identified several key considerations in determining the mass budget of large  
661 land-terminating glaciers. (1) The best assumption for determining depth-averaged velocity profiles for the  
662 purposes of calculating ice flux may vary spatially. (2) Bias corrections to modelled accumulation may



663 be large and spatially variable, due, for example, to orographic effects. Well-distributed accumulation  
664 measurements would be extremely valuable to characterize the accumulation field. (3) Incorporating  
665 processes such as refreezing, and properties such as debris cover, into mass-balance models can impart  
666 significant influence on the timing and magnitude of modelled melt. (4) Accounting for the effects of debris  
667 cover, especially at lower elevations, can significantly alter the modelled mass-balance gradient.

668 The mass balance of large and regionally significant glaciers like the Kaskawulsh Glacier remains  
669 impractical to measure with in-situ methods. We therefore need models like the one employed in this  
670 study, forced by spatially distributed glacio-meteorological data (e.g. reanalysis products, AWS timeseries,  
671 in-situ accumulation and ablation measurements), combined with creative ways to approach model tuning  
672 to characterize changing glacier mass budgets.

### 673 **SUPPLEMENTARY MATERIAL**

674 The supplementary material for this article can be found at <https://doi.org/xxxxxx>

### 675 **DATA AVAILABILITY**

676 The supplementary material for this article can be found at Data presented in this article are archived  
677 online on <https://xxxxxx>

### 678 **ACKNOWLEDGEMENTS**

679 Permission to conduct field work was granted by the Kluane First Nation (KFN), Parks Canada and  
680 Yukon Government. We are grateful to S. Williams, L. Goodwin and S. Shaw for logistical support, and D.  
681 Bigelow, C. Wong (Parks Canada) and U.H. Fischer for assistance in the field. L. Copland kindly provided  
682 temperature data used in the NARR bias corrections. We thank L. Mingo for assistance with interpretation  
683 of radar data, A. Adhikari for carrying out snowline picks, A. Morin for performing calculations involving the  
684 Farinotti and others (2019) dataset and H. Jiskoot for helpful discussions related to model tuning. SPOT6/7  
685 data were obtained thanks to public funds received in the framework of GEOSUD, a project (ANR-10-  
686 EQPX-20) of the program “Investissements d’Avenir” managed by the French National Research Agency.  
687 EB acknowledges support from the French Space Agency through the TOSCA and DINAMIS projects. We  
688 are grateful for financial support provided by the Natural Sciences and Engineering Research Council of  
689 Canada, Simon Fraser University, the Northern Scientific Training Program and the Polar Continental Shelf  
690 Program. The data presented in this manuscript will be made available upon acceptance.

691 **AUTHOR CONTRIBUTION STATEMENT**

692 GF conceived of the original study and EY/GF co-developed the details. EY developed, tuned and ran the  
693 mass-balance model, including all aspects of downloading/pre-processing model inputs, analyzing model  
694 output and integrating output with observations. EY also supervised Adhikari's work on snowlines. GF  
695 and EY carried out the field work. RL processed and interpreted the radar data with guidance from GF  
696 and calculated the ice fluxes with EY. EB acquired and processed the elevation-change data. EY led the  
697 manuscript preparation, with contributions from GF and EB. All authors contributed to various aspects of  
698 the interpretation and edited the manuscript.

For Peer Review

## 699 REFERENCES

- 700 Allen MR and 10 others (2014) IPCC fifth assessment synthesis report-climate change 2014 synthesis report
- 701 Anderton PW (1967) *Structural glaciology of a glacier confluence, Kaskawulsh Glacier, Yukon Territory, Canada*.  
702 Ph.D. thesis, The Ohio State University
- 703 Anderton PW (1973) *Structural glaciology of a glacier confluence, kaskawulsh glacier, yukon territory, canada*.  
704 Technical report, Research Foundation and the Institute of Polar Studies, The Ohio State University.
- 705 Arendt AA, Luthcke SB, Larsen CF, Abdalati W, Krabill WB and Beedle MJ (2008) Validation of high-resolution  
706 GRACE mascon estimates of glacier mass changes in the St Elias Mountains, Alaska, USA, using aircraft laser  
707 altimetry. *Journal of Glaciology*, **54**(188), 778–787 (doi: 10.3189/002214308787780067)
- 708 Azam MF and 10 others (2012) From balance to imbalance: a shift in the dynamic behaviour of Chhota Shigri glacier,  
709 western Himalaya, India. *Journal of Glaciology*, **58**(208), 315–324 (doi: 10.3189/2012JoG11J123)
- 710 Bachelder J and 10 others (2020) Chemical and microphysical properties of wind-blown dust near an actively retreat-  
711 ing glacier in Yukon, Canada. *Aerosol Science and Technology*, **54**(1), 2–20 (doi: 10.1080/02786826.2019.1676394)
- 712 Barrand N and Sharp M (2010) Sustained rapid shrinkage of Yukon glaciers since the 1957–1958 International  
713 Geophysical Year. *Geophysical Research Letters*, **37**(7) (doi: 10.1029/2009GL042030)
- 714 Benn D and 9 others (2012) Response of debris-covered glaciers in the Mount Everest region to recent  
715 warming, and implications for outburst flood hazards. *Earth-Science Reviews*, **114**(1-2), 156–174 (doi:  
716 10.1016/j.earscirev.2012.03.008)
- 717 Berthier É and Brun F (2019) Karakoram geodetic glacier mass balances between 2008 and 2016: persis-tence of the  
718 anomaly and influence of a large rock avalanche on Siachen Glacier. *Journal of Glaciology*, **65**(251), 494–507 (doi:  
719 10.1017/jog.2019.32)
- 720 Berthier E and Vincent C (2012) Relative contribution of surface mass-balance and ice-flux changes to the  
721 accelerated thinning of Mer de Glace, French Alps, over 1979–2008. *Journal of Glaciology*, **58**(209), 501–512  
722 (doi: 10.3189/2012JoG11J083)
- 723 Berthier E, Arnaud Y, Baratoux D, Vincent C and Rémy F (2004) Recent rapid thinning of the “Mer de Glace”  
724 glacier derived from satellite optical images. *Geophysical Research Letters*, **31**(17) (doi: 10.1029/2004GL020706)
- 725 Berthier E, Arnaud Y, Kumar R, Ahmad S, Wagnon P and Chevallier P (2007) Remote sensing estimates of glacier  
726 mass balances in the Himachal Pradesh (Western Himalaya, India). *Remote Sensing of Environment*, **108**(3),  
727 327–338 (doi: 10.1016/j.rse.2006.11.017)
- 728 Berthier E, Schiefer E, Clarke GKC, Menounos B and Rémy F (2010) Contribution of Alaskan glaciers to sea-level  
729 rise derived from satellite imagery. *Nature Geoscience*, **3**(2), 92 (doi: 10.1038/ngeo737)

- 730 Berthier E and 10 others (2014) Glacier topography and elevation changes derived from Pléiades sub-meter stereo  
731 images. *The Cryosphere*, **8**(6), 2275–2291 (doi: 10.5194/tc-8-2275-2014)
- 732 Bhattacharya A, Bolch T, Mukherjee K, Pieczonka T, Kropáček J and Buchroithner MF (2016) Overall recession  
733 and mass budget of Gangotri Glacier, Garhwal Himalayas, from 1965 to 2015 using remote sensing data. *Journal*  
734 *of Glaciology*, **62**(236), 1115–1133 (doi: 10.1017/jog.2016.96)
- 735 Bigelow DG (2019) *The role of englacial hydrology in the filling and drainage of an ice-dammed lake, Kaskawulsh*  
736 *Glacier, Yukon, Canada*. Master's thesis, Simon Fraser University
- 737 Bigelow DG, Flowers GE, Schoof CG, Mingo LDB, Young EM and Connal BC (2020) The role of englacial hydrology  
738 in the filling and drainage of an ice-dammed lake, Kaskawulsh Glacier, Yukon, Canada. *Journal of Geophysical*  
739 *Research: Earth Surface*, **125**(2) (doi: 10.1029/2019JF005110)
- 740 Bisset RR, Dehecq A, Goldberg DN, Huss M, Bingham RG and Gourmelen N (2020) Reversed surface-mass-balance  
741 gradients on Himalayan debris-covered glaciers inferred from remote sensing. *Remote Sensing*, **12**(10), 1563 (doi:  
742 10.3390/rs12101563)
- 743 Bogorodsky VV, Bentley CR and Gudmandsen PE (1985) *Radioglaciology*. D. Reidel Publishing Co., Dordrecht,  
744 Holland
- 745 Borns HW and Goldthwait RP (1966) Late-Pleistocene fluctuations of Kaskawulsh Glacier, southwestern Yukon  
746 Territory, Canada. *American Journal of Science*, **264**(8), 600–619 (doi: 10.2475/ajs.264.8.600)
- 747 Chinn T (1999) New Zealand glacier response to climate change of the past 2 decades. *Global and Planetary Change*,  
748 **22**(1-4), 155–168 (doi: 10.1016/S0921-8181(99)00033-8)
- 749 Clarke GKC (2014) A short and somewhat personal history of Yukon glacier studies in the Twentieth Century. *Arctic*,  
750 **67**, 1–21 (doi: 10.14430/arctic)
- 751 Clarke GKC and Holdsworth G (2002) Glaciers of the St. Elias mountains. *US Geological Survey professional paper*,  
752 (1386J)
- 753 Clarke GKC, Schmok JP, Ommanney CSL and Collins SG (1986) Characteristics of surge-type glaciers. *Journal of*  
754 *Geophysical Research: Solid Earth*, **91**(B7), 7165–7180 (doi: 10.1029/JB091iB07p07165)
- 755 Clarke GKC, Jarosch AH, Anslow FS, Radić V and Menounos B (2015) Projected deglaciation of western Canada  
756 in the twenty-first century. *Nature Geoscience*, **8**(5), 372 (doi: 10.1038/ngeo2407)
- 757 Cruikshank J (2001) Glaciers and climate change: perspectives from oral tradition. *Arctic*, 377–393
- 758 Cuffey KM and Paterson WSB (2010) *The physics of glaciers*. Elsevier
- 759 Darling S (2012) *Velocity Variations of the Kaskawulsh Glacier, Yukon Territory, 2009-2011*. University of Ottawa
- 760 De Woul M and Hock R (2005) Static mass-balance sensitivity of Arctic glaciers and ice caps using a degree-day  
761 approach. *Annals of Glaciology*, **42**, 217–224 (doi: 10.3189/172756405781813096)

- 762 Dehecq A and 9 others (2019) Twenty-first century glacier slowdown driven by mass loss in High Mountain Asia.  
763 *Nature Geoscience*, **12**(1), 22–27 (doi: 10.1038/s41561-018-0271-9)
- 764 Deschamps-Berger C, Nuth C, Van Pelt W, Berthier E, Kohler J and Altena B (2019) Closing the mass budget of a  
765 tidewater glacier: the example of Kronebreen, Svalbard. *Journal of Glaciology*, 1–13 (doi: 10.1017/jog.2018.98)
- 766 ECCC (2019a) Canada’s changing climate report. Technical report, Environment and Climate Change Canada,  
767 <https://changingclimate.ca/CCCR2019/>, date accessed: 29-05-2020
- 768 ECCC (2019b) Climate Trends and Variations Bulletin - Annual 2019. Technical report, Environment and Cli-  
769 mate Change Canada, [https://www.canada.ca/en/environment-climate-change/services/climate-change/science-](https://www.canada.ca/en/environment-climate-change/services/climate-change/science-research-data/climate-trends-variability/trends-variations/annual-2019-bulletin.html)  
770 [research-data/climate-trends-variability/trends-variations/annual-2019-bulletin.html](https://www.canada.ca/en/environment-climate-change/services/climate-change/science-research-data/climate-trends-variability/trends-variations/annual-2019-bulletin.html), date accessed: 29-05-2020
- 771 Farinotti D and 6 others (2019) A consensus estimate for the ice thickness distribution of all glaciers on Earth. *Nature*  
772 *Geoscience*, **12**(3), 168–173 (doi: 10.1038/s41561-019-0300-3)
- 773 Foy N, Copland L, Zdanowicz C, Demuth M and Hopkinson C (2011) Recent volume and area changes of Kaskawulsh  
774 Glacier, Yukon, Canada. *Journal of Glaciology*, **57**(203), 515–525 (doi: 10.3189/002214311796905596)
- 775 Gardner AS and 10 others (2013) A reconciled estimate of glacier contributions to sea level rise: 2003 to 2009. *science*,  
776 **340**(6134), 852–857 (doi: 10.1126/science.1234532)
- 777 Gardner AS and 6 others (2018) Increased West Antarctic and unchanged East Antarctic ice discharge over the last  
778 7 years. *Cryosphere*, **12**(2), 521–547 (doi: 10.5194/tc-12-521-2018)
- 779 Gardner AS, Fahnestock MA and Scambos TA (2019) ITS\_LIVE Regional Glacier and Ice Sheet Surface Velocities.  
780 Data archived at National Snow and Ice Data Center (doi: 10.5067/6II6VW8LLWJ7), data archived at National  
781 Snow and Ice Data Center
- 782 Guan H, Wilson JL and Makhnin O (2005) Geostatistical mapping of mountain precipitation incorporating  
783 autosearched effects of terrain and climatic characteristics. *Journal of Hydrometeorology*, **6**(6), 1018–1031 (doi:  
784 10.1175/JHM448.1)
- 785 Guan H, Wilson JL and Xie H (2009) A cluster-optimizing regression-based approach for precipitation spatial  
786 downscaling in mountainous terrain. *Journal of Hydrology*, **375**(3-4), 578–588 (doi: 10.1016/j.jhydrol.2009.07.007)
- 787 Hay LE, Wilby RL and Leavesley GH (2000) A comparison of delta change and downscaled GCM scenarios for three  
788 mountainous basins in the United States 1. *JAWRA Journal of the American Water Resources Association*, **36**(2),  
789 387–397 (doi: 10.1111/j.1752-1688.2000.tb04276.x)
- 790 Herdes E (2014) *Evolution of seasonal variations in motion of the Kaskawulsh Glacier, Yukon Territory*. Ph.D. thesis,  
791 University of Ottawa
- 792 Hock R (1998) *Modelling of glacier melt and discharge*. Ph.D. thesis, ETH Zurich
- 793 Hock R (1999) A distributed temperature-index ice-and snowmelt model including potential direct solar radiation.  
794 *Journal of Glaciology*, **45**(149), 101–111 (doi: 10.3189/S0022143000003087)

- 795 Hock R and 7 others (2019) GlacierMIP—A model intercomparison of global-scale glacier mass-balance models and  
796 projections. *Journal of Glaciology*, **65**(251), 453–467 (doi: <https://doi.org/10.1017/jog.2019.22>)
- 797 Hofer M, Nemeč J, Cullen NJ and Weber M (2017) Evaluating predictor strategies for regression-based downscaling  
798 with a focus on glacierized mountain environments. *Journal of Applied Meteorology and Climatology*, **56**(6), 1707–  
799 1729 (doi: [10.1175/JAMC-D-16-0215.1](https://doi.org/10.1175/JAMC-D-16-0215.1))
- 800 Holdsworth G (1965) An examination and analysis of the formation of transverse crevasses, Kaskawulsh Glacier,  
801 Yukon Territory, Canada. Technical report, Institute of Polar Studies, The Ohio State University.
- 802 Huss M (2013) Density assumptions for converting geodetic glacier volume change to mass change. *The Cryosphere*,  
803 **7**(3), 877–887 (doi: [10.5194/tc-7-877-2013](https://doi.org/10.5194/tc-7-877-2013))
- 804 Huss M, Funk M and Ohmura A (2009) Strong alpine glacier melt in the 1940s due to enhanced solar radiation.  
805 *Geophysical Research Letters*, **36**(23) (doi: [10.1029/2009GL040789](https://doi.org/10.1029/2009GL040789))
- 806 Janssens I and Huybrechts P (2000) The treatment of meltwater retention in mass-balance parameterizations of the  
807 Greenland ice sheet. *Annals of Glaciology*, **31**, 133–140 (doi: [10.3189/172756400781819941](https://doi.org/10.3189/172756400781819941))
- 808 Jarosch AH, Anslow FS and Clarke GKC (2012) High-resolution precipitation and temperature downscaling for  
809 glacier models. *Climate Dynamics*, **38**(1-2), 391–409 (doi: [10.1007/s00382-010-0949-1](https://doi.org/10.1007/s00382-010-0949-1))
- 810 Johannesson T, Sigurdsson O, Laumann T and Kennett M (1995) Degree-day glacier mass-balance modelling  
811 with applications to glaciers in Iceland, Norway and Greenland. *Journal of Glaciology*, **41**(138), 345–358 (doi:  
812 [10.3189/S0022143000016221](https://doi.org/10.3189/S0022143000016221))
- 813 Johnson P (1972) A possible advanced hypsithermal position of the Donjek Glacier. *Arctic*, **25**(4), 302–305
- 814 Kelsey EP, Wake CP, Yalcin K and Kreutz K (2012) Eclipse ice core accumulation and stable isotope variability as  
815 an indicator of North Pacific climate. *Journal of Climate*, **25**(18), 6426–6440 (doi: [10.1175/JCLI-D-11-00389.1](https://doi.org/10.1175/JCLI-D-11-00389.1))
- 816 Kienholz C, Herreid S, Rich JL, Arendt AA, Hock R and Burgess EW (2015) Derivation and analysis of a complete  
817 modern-date glacier inventory for Alaska and northwest Canada. *Journal of Glaciology*, **61**(227), 403–420 (doi:  
818 [10.3189/2015JoG14J230](https://doi.org/10.3189/2015JoG14J230))
- 819 Kienzle SW (2008) A new temperature based method to separate rain and snow. *Hydrological Processes: An*  
820 *International Journal*, **22**(26), 5067–5085 (doi: [10.1002/hyp.7131](https://doi.org/10.1002/hyp.7131))
- 821 Korona J, Berthier E, Bernard M, Rémy F and Thouvenot E (2009) Spirit. SPOT 5 stereoscopic survey of polar  
822 ice: reference images and topographies during the fourth International Polar Year (2007–2009). *ISPRS Journal of*  
823 *Photogrammetry and Remote Sensing*, **64**(2), 204–212 (doi: [10.1016/j.isprsjprs.2008.10.005](https://doi.org/10.1016/j.isprsjprs.2008.10.005))
- 824 Krieger G and 6 others (2007) TanDEM-X: A satellite formation for high-resolution SAR interferometry. *IEEE*  
825 *Transactions on Geoscience and Remote Sensing*, **45**(11), 3317–3341 (doi: [10.1109/TGRS.2007.900693](https://doi.org/10.1109/TGRS.2007.900693))
- 826 Lacroix P (2016) Landslides triggered by the Gorkha earthquake in the Langtang valley, volumes and initiation  
827 processes. *Earth, Planets and Space*, **68**(1), 46 (doi: [10.1186/s40623-016-0423-3](https://doi.org/10.1186/s40623-016-0423-3))

- 828 Langhammer L, Grab M, Bauder A and Maurer H (2019) Glacier thickness estimations of alpine glaciers using data  
829 and modeling constraints. *The Cryosphere*, **13**, 2189–2202 (doi: 10.3929/ethz-b-000361623)
- 830 Larsen C, Burgess E, Arendt A, O’neel S, Johnson A and Kienholz C (2015) Surface melt dominates Alaska glacier  
831 mass balance. *Geophysical Research Letters*, **42**(14), 5902–5908 (doi: 10.1002/2015GL064349)
- 832 Marcus MG and Ragle RH (1970) Snow accumulation in the Icefield Ranges, St. Elias Mountains, Yukon. *Arctic and  
833 Alpine Research*, **2**(4), 277–292 (doi: 10.1080/00040851.1970.12003587)
- 834 McKnight E (2017) Characterizing and monitoring the water properties and dynamics of Lhù’àn Män (Kluane  
835 Lake), Yukon, in the face of climate change. *Arctic*, **70**(4), 435–440
- 836 McNabb R, Nuth C, Käab A and Girod L (2019) Sensitivity of glacier volume change estimation to DEM void  
837 interpolation. *The Cryosphere*, **13**(3), 895–910 (doi: 10.5194/tc-13-895-2019)
- 838 Meier MF and Tangborn WV (1965) Net budget and flow of South Cascade glacier, Washington. *Journal of  
839 Glaciology*, **5**(41), 547–566 (doi: 10.3189/S0022143000018608)
- 840 Meier MF and 7 others (2007) Glaciers dominate eustatic sea-level rise in the 21st century. *Science*, **317**(5841),  
841 1064–1067 (doi: 10.1126/science.1143906)
- 842 Mernild SH, Lipscomb WH, Bahr DB, Radić V and Zemp M (2013) Global glacier changes: a revised assessment of  
843 committed mass losses and sampling uncertainties. *The Cryosphere*, **7**(5), 1565–1577 (doi: 10.5194/tc-7-1565-2013)
- 844 Mesinger F and 10 others (2006) North American regional reanalysis. *Bulletin of the American Meteorological Society*,  
845 **87**(3), 343–360 (doi: 10.1175/BAMS-87-3-343)
- 846 Mingo L and Flowers GE (2010) An integrated lightweight ice-penetrating radar system. *Journal of Glaciology*,  
847 **56**(198), 709–714 (doi: 10.3189/002214310793146179)
- 848 Mingo L, Flowers GE, Crawford AJ, Mueller D and Bigelow D (2020) A stationary impulse-radar system for au-  
849 tonomous deployment in cold and temperature environments. *Annals of Glaciology*, 1–9 (doi: 10.1017/aog.2020.2)
- 850 Nakao M (1982) *A simplified model for estimating glacier ablation under a debris layer*. International Association of  
851 Hydrological Sciences
- 852 Narod BB and Clarke GKC (1994) Miniature high-power impulse transmitter for radio-echo sounding. *Journal of  
853 Glaciology*, **40**(134), 190–194 (doi: 10.3189/S002214300000397X)
- 854 Nuth C and Käab A (2011) Co-registration and bias corrections of satellite elevation data sets for quantifying glacier  
855 thickness change. *The Cryosphere*, **5**(1), 271–290 (doi: 10.5194/tc-5-271-2011)
- 856 Nye JF (1965) The flow of a glacier in a channel of rectangular, elliptic or parabolic cross-section. *Journal of  
857 Glaciology*, **5**(41), 661–690 (doi: 10.3189/S0022143000018670)
- 858 Oerlemans J (1991) The mass balance of the greenland ice sheet: sensitivity to climate change as revealed by energy-  
859 balance modelling. *The Holocene*, **1**(1), 40–48 (doi: 10.1177/095968369100100106)

- 860 Paul F and 10 others (2015) The glaciers climate change initiative: Methods for creating glacier area, elevation  
861 change and velocity products. *Remote Sensing of Environment*, **162**, 408–426 (doi: 10.1016/j.rse.2013.07.043)
- 862 Pelto MS and 6 others (2008) The equilibrium flow and mass balance of the Taku Glacier, Alaska 1950–2006. *The*  
863 *Cryosphere*, **2**(2), 147–157 (doi: 10.5194/tc-2-147-2008)
- 864 Pfeffer WT and 10 others (2014) The Randolph Glacier Inventory: a globally complete inventory of glaciers. *Journal*  
865 *of Glaciology*, **60**(221), 537–552 (doi: 10.3189/2014JoG13J176)
- 866 Post A (1969) Distribution of surging glaciers in western North America. *Journal of Glaciology*, **8**(53), 229–240 (doi:  
867 10.3189/S0022143000031221)
- 868 Radić V, Bliss A, Beedlow AC, Hock R, Miles E and Cogley JG (2014) Regional and global projections of twenty-  
869 first century glacier mass changes in response to climate scenarios from global climate models. *Climate Dynamics*,  
870 **42**(1-2), 37–58 (doi: 10.1007/s00382-013-1719-7)
- 871 Raup B, Racoviteanu A, Khalsa SJS, Helm C, Armstrong R and Arnaud Y (2007) The GLIMS geospatial  
872 glacier database: a new tool for studying glacier change. *Global and Planetary Change*, **56**(1-2), 101–110 (doi:  
873 10.1016/j.gloplacha.2006.07.018)
- 874 Reyes AV, Luckman BH, Smith DJ, Clague JJ and Van Dorp RD (2006) Tree-ring dates for the maximum Little Ice  
875 Age advance of Kaskawulsh Glacier, St. Elias Mountains, Canada. *Arctic*, **59**(1), 14–20
- 876 Reznichenko N, Davies T, Shulmeister J and McSaveney M (2010) Effects of debris on ice-surface melting rates: an  
877 experimental study. *Journal of Glaciology*, **56**(197), 384–394 (doi: 10.3189/002214310792447725)
- 878 RGI Consortium (2017) Randolph Glacier Inventory—a dataset of global glacier outlines: Version 6.0: technical report,  
879 global land ice measurements from space, Colorado, USA. *Digital Media*
- 880 Rizzoli P and 10 others (2017) Generation and performance assessment of the global TanDEM-X digital elevation  
881 model. *ISPRS Journal of Photogrammetry and Remote Sensing*, **132**, 119–139 (doi: 10.1016/j.isprsjprs.2017.08.008)
- 882 Sælthun N (1996) The ‘Nordic’HBV model. Description and documentation of the model version developed for the  
883 project climate change and energy production. *NVE publication*, **7**
- 884 Shean DE and 6 others (2016) An automated, open-source pipeline for mass production of digital elevation models  
885 (DEMs) from very-high-resolution commercial stereo satellite imagery. *ISPRS Journal of Photogrammetry and*  
886 *Remote Sensing*, **116**, 101–117 (doi: 10.1016/j.isprsjprs.2016.03.012)
- 887 Shugar DH and 6 others (2017) River piracy and drainage basin reorganization led by climate-driven glacier retreat.  
888 *Nature Geoscience*, **10**(5), 370 (doi: 10.1038/ngeo2932)
- 889 Smith RB and Barstad I (2004) A linear theory of orographic precipitation. *Journal of the Atmospheric Sciences*,  
890 **61**(12), 1377–1391 (doi: 10.1175/1520-0469(2004)061<1377:ALTOOP>2.0.CO;2)
- 891 Span N and Kuhn M (2003) Simulating annual glacier flow with a linear reservoir model. *Journal of Geophysical*  
892 *Research: Atmospheres*, **108**(D10) (doi: 10.1029/2002JD002828)



- 893 Streicker J (2016) Yukon climate change indicators and key findings 2015. *Whitehorse: Northern Climate Exchange,*  
894 *Yukon Research Centre, Yukon College*
- 895 Thomson LI, Zemp M, Copland L, Cogley JG and Ecclestone MA (2017) Comparison of geodetic and glaciological  
896 mass budgets for White Glacier, Axel Heiberg Island, Canada. *Journal of Glaciology*, **63**(237), 55–66
- 897 Vaughan DG and 10 others (2013) Observations: cryosphere. *Climate change*, **2103**, 317–382
- 898 Vincent C and Six D (2013) Relative contribution of solar radiation and temperature in enhanced temperature-  
899 index melt models from a case study at Glacier de Saint-Sorlin, France. *Annals of glaciology*, **54**(63), 11–17 (doi:  
900 10.3189/2013AoG63A301)
- 901 Vincent C and 10 others (2016) Reduced melt on debris-covered glaciers: investigations from Changri Nup Glacier,  
902 Nepal. *The Cryosphere*, **10**, 1845–1858 (doi: 10.5194/tc-10-1845-2016)
- 903 Wild M and 9 others (2005) From dimming to brightening: Decadal changes in solar radiation at Earth's surface.  
904 *Science*, **308**(5723), 847–850 (doi: 10.1126/science.1103215)
- 905 Williamson SN and 9 others (2020) Evidence for elevation-dependent warming in the St. Elias Mountains, Yukon,  
906 Canada. *Journal of Climate*, **33**(8), 3253–3269 (doi: 10.1175/JCLI-D-19-0405.1)
- 907 Wilson NJ (2012) *Characterization and interpretation of polythermal structure in two subarctic glaciers*. Master's  
908 thesis, Simon Fraser University
- 909 Wilson NJ, Flowers GE and Mingo L (2013) Comparison of thermal structure and evolution between neighboring  
910 subarctic glaciers. *Journal of Geophysical Research: Earth Surface*, **118**(3), 1443–1459, ISSN 21699011 (doi:  
911 10.1002/jgrf.20096)
- 912 Wouters B, Gardner AS and Moholdt G (2019) Global glacier mass loss during the GRACE satellite mission (2002-  
913 2016). *Frontiers in earth science*, **7** (doi: 10.3389/feart.2019.00096)
- 914 Zemp M and 10 others (2019) Global glacier mass changes and their contributions to sea-level rise from 1961 to 2016.  
915 *Nature*, **568**(7752), 382 (doi: 10.1038/s41586-019-1071-0)